International Journal of Modern Physics C
Vol. 31, No. 9 (2020) 2050131 (44 pages)

DOI: 10.1142/S0129183120501314

World Scientific
www.worldscientific.com

Energy spectrum of two-particle scattering in a periodic box

Frank X. Lee*,‡, Colin Morningstar†,§ and Andrei Alexandru*,¶

*Physics Department, The George Washington University
Washington, DC 20052, USA

†Department of Physics, Carnegie Mellon University
Pittsburgh, Pennsylvania 15213, USA
‡fxlee@gwu.edu
§cmorning@andrew.cmu.edu
¶aalexan@gwu.edu

Received 29 December 2019
Accepted 19 May 2020
Published 15 August 2020

We aim to compute the discrete energy spectrum for two-body scattering in a three-dimensional box under periodic boundary conditions. The spectrum in the center of mass is obtained by solving the Schödinger equation in a test potential using the Fourier basis. The focus is on how to project the spectrum into the various irreducible representations of the symmetry groups of the box. Four examples are given to show how the infinite-volume spectrum (including both bound and scattering states) is resolved in cubic or elongated boxes, and in systems with integer or half-integer total spin. Such a demonstration is a crucial step in relating the discrete spectrum in the box to the infinite-volume scattering phaseshifts via the Lüscher method.

Keywords: Two-body scattering; cubic and elongated boxes; periodic boundary conditions; Fourier basis; irreducible representations.

1. Introduction

Scattering is an indispensable tool in probing the nature of interactions between two particles, either in atomic and molecular physics or in nuclear and particle physics. An effective theoretical method is the use of a finite box to enclose the system under consideration. The energy of the system is quantized in the box. Scattering resonance parameters can be extracted from the energy spectrum as a function of the box size. In the early days, the method was applied mostly to one-dimensional systems and Dirichlet boundary conditions (for an example see Ref. 1). The breakthrough came in the seminal work by Lüscher[2] that established exact relations between elastic scattering phaseshifts and the two-body energy spectrum enclosed in a three-dimensional box with periodic boundary conditions. Such relations (also known as quantization conditions) are fairly general: it does not matter how the energy spectrum is

‡Corresponding author.

obtained. The method is known as the Lüscher method and has been successfully applied in the field of lattice QCD to obtain resonance parameters in hadron–hadron scattering in terms of quark–gluon dynamics. In lattice QCD, the energy is computed from path integrals on a periodic space-time lattice in large-scale Monte-Carlo simulations. Since then, various extensions to the Lüscher method have been made to widen its applications, including moving frames,[3] spin-1/2 particles,[4] higher partial waves,[5] asymmetric boxes,[6,7] inelastic scattering,[8,9] partial-wave mixing in Hamiltonian effective theory,[10] three-body systems,[11,12] and matrix elements.[13]

In numerical simulations in a periodic box, the standard method to obtain the energy spectrum is to discretize the box L^3 into a lattice N^3a^3. To remove the discretization errors, one takes the continuum limit of $a \to 0$ and $L \to \infty$ while keeping the size $L = Na$ fixed. Here, we present an alternative method without discretization. We use a Fourier basis to compute the energy spectrum. We show how to apply group theory to the basis to take full account of the symmetry of the box. We want the framework to be as pedagogical as possible so the techniques can be applied to a wider range of problems. We employ both cubic and elongated boxes. The use of elongated boxes has shown promise in reducing the cost of lattice QCD simulations.[14,15] We consider systems of not only integer spin, but also half-integer spin which is drawing increasing interest.[16] Since the Lüscher method applies regardless of how the interaction energy is obtained in the box, we use a simple potential model in nonrelativistic quantum mechanics and focus only on the two-body energy spectrum. To facilitate the application of the methods we decide to make the entire framework available as a computational package.[a]

The presentation is organized as follows. After the infinite-volume spectrum is introduced in Sec. 2, the discrete energy spectrum is discussed in four sections: spin-0 and cubic box in Sec. 3.1, spin-1/2 and cubic box in Sec. 3.3, spin-0 and elongated box in Sec. 4.1, spin-1/2 and elongated box in Sec. 4.2. Some technical details are relegated to the three appendices.

2. Scattering in Infinite Volume

The standard method for two-body scattering in the continuum is to separate it into the total motion of center of mass (CM) and the relative motion in the CM. In the CM frame, it is a one-body Schrödinger equation problem

$$\left[-\frac{\hbar^2}{2\mu}\nabla^2 + V(r)\right]\psi(\boldsymbol{r}) = E\psi(\boldsymbol{r}), \tag{1}$$

where $\mu = m_1 m_2/(m_1 + m_2)$ is the reduced mass, and $V(r)$ a local, energy-independent potential.

[a] The package is written in C++ and Mathematica and can be obtained from the authors upon request.

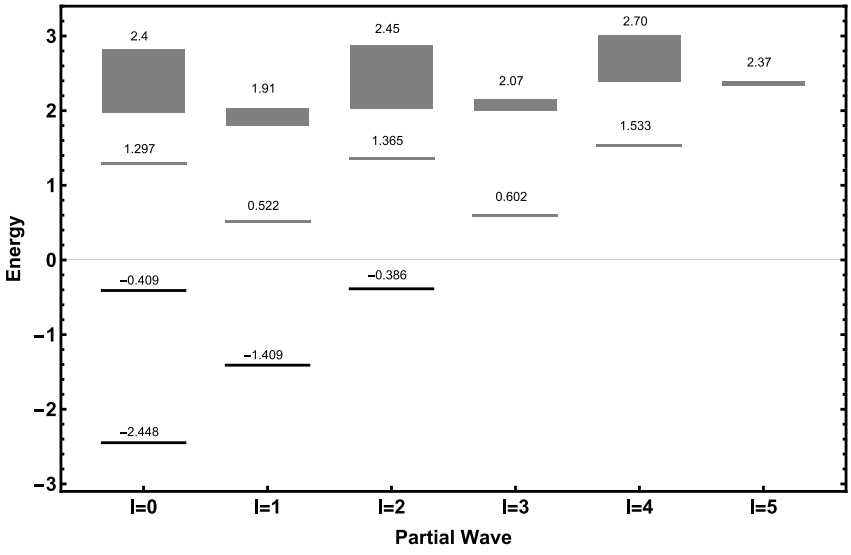

Fig. 1. Low-lying energy spectrum allowed by the spin-0 potential in Eq. (2) in the infinite volume for $E < 3$ and $l \leq 5$. Bound states are indicated by a minus sign. Resonances are indicated by the center position and shaded width.

In this study, we consider two cases for the interaction potential. First is the scattering of two spinless particles (hereafter referred to as the spin-0 system) of either equal or unequal masses. We work with a dimensionless Hamiltonian $H = -\frac{1}{2}\nabla^2 + V(r)$ in the unit system $\hbar = c = \mu = 1$, with a dimensionless potential and dimensionless distance r,

$$V(r) = (-V_0 + V_1 r^4) e^{-\beta r^2}, \tag{2}$$

where $V_0 = 4$, $V_1 = 1/16$, and $\beta = 1/8$. This potential has a mixture of bound states and narrow and wide resonances, suitable for testing purposes. Figure 1 shows the low-lying energy spectrum admitted by the potential. It has four bound states across three partial waves, and over 10 resonances with varying widths, in the range $E < 3$ and $l \leq 5$. Details on how the states are found are given in Appendix A.

The second case is scattering of a spinless particle and a spin-1/2 particle (hereafter referred to as the spin-1/2 system). The potential now has a spin-orbit coupling term added to the spin-zero case,

$$V_{Jl}(r) = (-V_0 + V_1 r^4 + c_{\ell s}\, \boldsymbol{\ell} \cdot \boldsymbol{s}) e^{-\beta r^2}. \tag{3}$$

We use the same parameters $V_0 = 4$, $V_1 = 1/16$, and $\beta = 1/8$ for the central part. The wavefunction is the eigenstate of $\{\boldsymbol{J}^2, J_z, \boldsymbol{\ell}^2, \boldsymbol{s}^2\}$ which we label as $|JM\ell\rangle$. In spherical coordinates, it has the form $\psi(\boldsymbol{r}) = R_\ell(r)\mathcal{Y}_{JM\ell}(\theta, \phi)$ where $\mathcal{Y}_{JM\ell}$ is the two-component spin spherical harmonics. The total angular momentum is $\boldsymbol{J} = \boldsymbol{\ell} + \boldsymbol{s}$.

For a given partial wave ℓ (except s-wave), there are two possible J values: $J_\pm = \ell \pm 1/2$. The spin-orbit coupling in this basis becomes

$$\ell \cdot \boldsymbol{s} = \frac{1}{2}\left[J(J+1) - \ell(\ell+1) - \frac{3}{4}\right] = \begin{cases} \ell/2 & \text{for } J = \ell + \dfrac{1}{2} \\ -(\ell+1)/2 & \text{for } J = \ell - \dfrac{1}{2} \quad (\ell \neq 0). \end{cases} \tag{4}$$

The potential is diagonal in this basis

$$V_{J\ell}(r) = \begin{pmatrix} V_{J=\ell+\frac{1}{2}}(r) & 0 \\ 0 & V_{J=\ell-\frac{1}{2}}(r) \end{pmatrix}. \tag{5}$$

Thus for each partial wave l, the two states $J = \ell \pm \frac{1}{2}$ can be treated separately in the infinite volume. In the finite volume, however, the two remain coupled as in Eq. (3), as we will see later. The two potentials are

$$V_{J=\ell+\frac{1}{2}}(r) = \left(-V_0 + V_1 r^4 + \frac{1}{2}\ell c_{\ell s}\right) e^{-\beta r^2}, \tag{6}$$

$$V_{J=\ell-\frac{1}{2}}(r) = \left(-V_0 + V_1 r^4 - \frac{1}{2}(\ell+1) c_{\ell s}\right) e^{-\beta r^2}. \tag{7}$$

We see that the effect of the spin-orbit term is to modify the V_0 value. As ℓ increases, the potential $V_{J=\ell+\frac{1}{2}}(r)$ is less and less likely to support bound states and resonances. On the other hand, the depth of $V_{J=\ell-\frac{1}{2}}(r)$ grows with ℓ so it is more and more likely to support bound states and resonances, although this effect is offset by the increasing centrifugal barrier. Plotting these potentials for low-lying values of ℓ for a variety of $c_{\ell s}$ values leads us to conclude that a value of $c_{\ell s}$ on the order of unity introduces noticeable but not overwhelmingly large changes to the spectrum compared to the spin-zero case. We shall use $c_{s\ell} = 1.0$ for our test.

Figure 2 shows the energy spectrum of this potential in the range $E < 3$ and $l \leq 7$. The system has seven bound states, two more than the spin-0 system, including a very shallow state at $E = -0.061$. It has about 20 resonances in the given range, some of them very sharp. Note that two more partial waves are included compared to the spin-0 case.

Our primary objective is to see how to reproduce these infinite-volume states in a periodic box.

3. Spectrum in Cubic Box

In infinite-volume (which we also refer to as continuum in this study), the problem is spherically symmetric. When confined in a cubic box, however, the spherical symmetry is broken by the geometry of the box. Furthermore, for scattering states the energy spectrum is quantized due to the fact that the back-to-back momentum is a

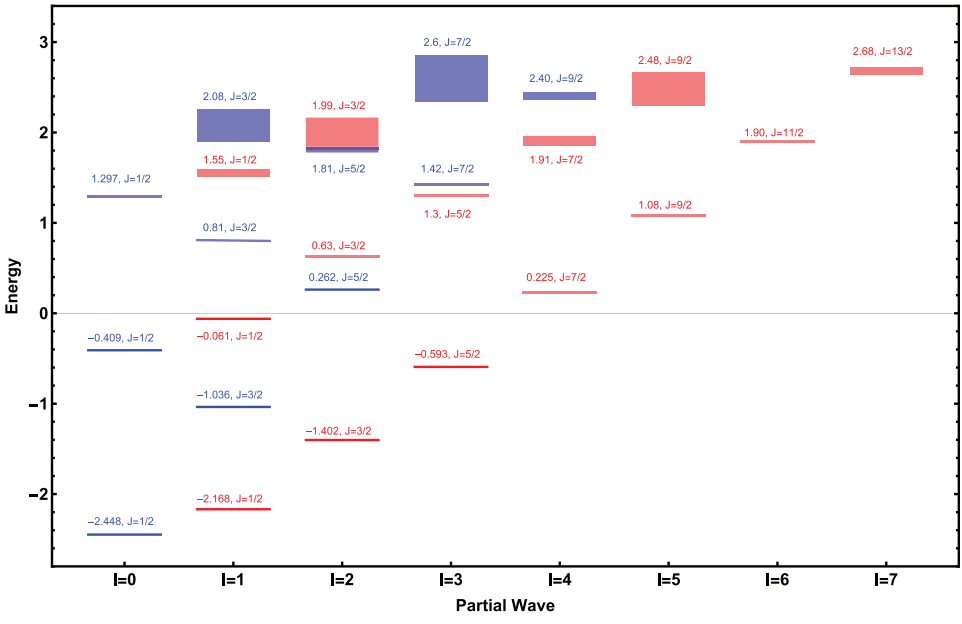

Fig. 2. (Color online) Low-lying energy spectrum admitted by the spin-1/2 potentials in Eqs. (6) and (7) in the infinite volume for $E < 3$ and $\ell \leq 7$. For a given partial wave ℓ, there are two possible J values, $J = \ell + 1/2$ (blue) and $J = \ell - 1/2$ (red).

multiple of $2\pi/L$ where L is the box size. The bound states, on the other hand, should not be affected too much as long as the box size is bigger than the range of the interaction potential. The goal here is to obtain the discrete energy spectrum in the box, and identify bound and scattering states while fully respecting the symmetry of the box.

3.1. *Spin-0 system*

We want to solve the Schrödinger equation in a cubic box centered on the origin with periodic boundary conditions.[b] In Cartesian coordinates, Eq. (1) takes the form

$$\left[-\frac{\hbar^2}{2\mu}\left(\frac{\partial^2}{\partial x^2}+\frac{\partial^2}{\partial y^2}+\frac{\partial^2}{\partial z^2}\right)+V_L(x,y,z)\right]\psi(x,y,z)=E\psi(x,y,z), \tag{8}$$

where the potential becomes periodic

$$V_L(,x,y,z)=\sum_{n_x,n_y,n_z} V(|(x+n_xL,y+n_yL,z+n_zL)|). \tag{9}$$

Visually, the continuous space gets tiled into an infinite number of L^3 boxes in which the potential is replicated. Under this scenario, the potential is no longer

[b]Since the system is translationally invariant, the results do not depend on where to place the origin.

rotationally symmetric. Instead, it takes on the symmetry of the box. The wavefunctions satisfy the periodic boundary conditions

$$\psi(x + n_x L, y + n_y L, z + n_z L) = \psi(x, y, z), \tag{10}$$

for integers (n_x, n_y, n_z). It is important to point out that this form of periodic boundary condition assumes that the total momentum $\boldsymbol{P} = \boldsymbol{p}_1 + \boldsymbol{p}_2$ of the two-particle system is zero in the rest frame of the box (lab frame). This means that the particles have equal and opposite momenta ($\boldsymbol{p}_1 = -\boldsymbol{p}_2 = \boldsymbol{k}$) in both the lab and CM frames (or the two frames coincide). For moving frames ($\boldsymbol{P} \neq 0$), a modified boundary condition is required (see Ref. 3 for example). Solving moving frames is beyond the scope of this work. We will only consider the rest frame ($\boldsymbol{P} = 0$).

The energy and momentum are related by the dispersion relation $E = \frac{\hbar^2 k^2}{2\mu}$. For a free particle in the periodic box, the momentum is quantized as $\boldsymbol{k} = \frac{2\pi}{L}\{n_x, n_y, n_z\}$ so the energy is quantized. In the presence of interactions, the dispersion relation still holds, but E and k deviate from the free-particle values. It is these deviations that encode information about the interaction in terms of phaseshifts or scattering lengths.

There are different ways to obtain the discreet energy spectrum in the cubic box. We choose to work with a Fourier basis as a variational basis to diagonalize the Hamiltonian. In one dimension, the basis is given by

$$\langle x|n_x\rangle = \phi_{n_x}(x, L) = \begin{cases} \sqrt{\dfrac{2}{L(1+\delta_{n_x 0})}} \cos\left(\dfrac{2\pi n_x x}{L}\right) & \text{for } n_x = 0, 1, 2, \ldots \\ \sqrt{\dfrac{2}{L}} \sin\left(\dfrac{2\pi n_x x}{L}\right) & \text{for } n_x = 1, 2, 3, \ldots \end{cases} \tag{11}$$

It is an orthonormal and complete basis; any function can be expanded in this basis. We need its form in three dimensions:

$$\langle x, y, z|n_x n_y n_z\rangle = \phi_{n_x}(x, L)\phi_{n_y}(y, L)\phi_{n_z}(z, L). \tag{12}$$

The basis naturally satisfies the periodic boundary conditions specified in Eq. (10). Expanding the wavefunction in this variational basis,

$$\psi(x, y, z) = \sum v_{n_x n_y n_z} \phi_{n_x}(x, L)\phi_{n_y}(y, L)\phi_{n_z}(z, L), \tag{13}$$

leads to the eigenvalue problem in matrix form $Hv = Ev$ where the Hamiltonian matrix elements are given by the integrals

$$\begin{aligned} \langle n'_x n'_y n'_z|\hat{H}|n_x n_y n_z\rangle = & \int_{-L/2}^{L/2} dx \int_{-L/2}^{L/2} dy \int_{-L/2}^{L/2} dz\ \phi_{n'_x}(x, L)\phi_{n'_y}(y, L)\phi_{n'_z}(z, L) \\ & \times \hat{H}\phi_{n_x}(x, L)\phi_{n_y}(y, L)\phi_{n_z}(z, L). \end{aligned} \tag{14}$$

The eigenvalues $\{E\}$ are the discrete energies allowed in the box. The eigenvectors $\{v\}$ yield the superposition coefficients for the corresponding wavefunctions. In the

spirit of variational principle, better convergence on the lower part of the spectrum can be achieved by including more Fourier modes in the basis. In practice, one can adjust the number of modes to achieve a desired accuracy.

One issue is if the system has bound states, a very large basis (several thousand) is required to achieve convergence. The reason is that bound states have wavefunctions which are very localized near the origin. The expansions of such wavefunctions in terms of the Fourier modes converge very slowly. It takes many Fourier modes to build up the localized wave functions of the bound states. A solution to this problem is to include localized states in our basis. We apply the damping factor $e^{-\gamma r^2}$ on the basis functions with the adjustable parameter γ to control the damping rate. The damped Fourier modes are no longer orthogonal so we need to solve a generalized eigenvalue problem $Hv = EBv$ where $B = \langle \gamma' n'_x n'_y n'_z | \gamma n_x n_y n_z \rangle$ is the overlap matrix between the basis states. We intend to include a fairly large number of undamped basis states ($\gamma = 0$) to capture the scattering stationary states. To reproduce the few bound states, we add a few states with γ chosen to match the extent of the bound states. The damped Fourier modes have the same transformation properties as the undamped Fourier modes under rotations and reflections, but their presence breaks the periodic boundary conditions in the undamped Fourier modes. We choose γ to be sufficiently large to ensure that these functions are localized near the origin and negligible near the box boundaries, so these functions can be made periodic in the same manner as the potential was made periodic. For the test potentials in this study, the matrix elements involved are all analytical. Details of their evaluations are relegated to Appendix C.

3.2. *Block diagonalization*

We want to apply group theory to diagonalize the Hamiltonian matrix. First we briefly review the terminology of the cubic symmetry. There are 24 elements for the cubic box that form the octahedral group O, as depicted in Fig. 3.

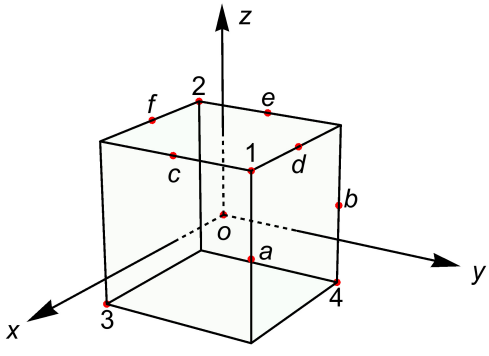

Fig. 3. The cubic box is invariant under 24 rotations about the various axes, as explained in the text.

They are divided into five groups (called conjugacy classes) and are given conventional names: the identity (E); six $\pi/2$ rotations about Cartesian axes ($C_{4x}^{\pm}$, $C_{4y}^{\pm}$, $C_{4z}^{\pm}$); three π rotations about Cartesian axes (C_{2x}, C_{2y}, C_{2z}); eight $2\pi/3$ rotations about body diagonals ($C_{31}^{\pm}$, $C_{32}^{\pm}$, $C_{33}^{\pm}$, $C_{34}^{\pm}$); and six π rotations about axes parallel to face diagonals (C_{2a}, C_{2b}, C_{2c}, C_{2d}, C_{2e}, C_{2f}). The operations are performed in a right-hand way with the thumb pointing from the center to the various symmetry points. The O group has five irreducible representations (irreps) named A_1, A_2, E, T_1, T_2 with respective dimensionality of $1, 1, 2, 3, 3$. In addition to the rotations, space inversion (parity) is also a symmetry of the cubic box. The full symmetry group including parity is called O_h which has 48 elements and 10 irreps $A_1^{\pm}$, $A_2^{\pm}$, $E^{\pm}$, $T_1^{\pm}$, $T_2^{\pm}$. Sometimes even and odd parity are represented by German words *gerade* or *ungerade*, respectively. For example, A_1^+ is $A1g$, and A_1^- is $A1u$, and so on. We use these two notations interchangeably in the entire package. More details about the cubic group can be found in our previous work Ref. 7.

In group theory, the rotationally-symmetric continuum is represented by the $SO(3)$ which has an infinite sequence of $2J+1$ irreps (whose basis vectors are spherical harmonics Y_{JM}) classifying integer angular momentum $J = 0, 1, 2, 3, \ldots$. In the cubic box, however, only 10 possibilities exist for the classification of integer angular momentum: the 10 irreps of the O_h group, shown in Table 1.

A straightforward diagonalization of the Hamiltonian in the Fourier basis yields eigenstates that are a mixture of the irreps and partial waves. One then has to disentangle the states as to which irreps they belong with what angular momentum. For a large basis, the computation becomes both memory and time intensive. A more efficient approach is to work on the Fourier basis before diagonalization. We need to construct the Fourier basis vectors (a linear superposition of the Fourier modes $|n_x n_y n_z\rangle$) that transform according to the property of the irreps. The Hamiltonian

Table 1. Decomposition of integer angular momentum in the cubic box according to the irreps of the O_h group. Both the original decomposition (left) and its inverse (right) are shown. The number in parentheses indicates the multiplicity of that J in that irrep.

J	O_h	O_h	J
0	A_1^+	A_1^+	0, 4, 6, ...
1	T_1^-	A_1^-	9, 13, 15, ...
2	$T_2^+ \oplus E^+$	T_1^-	1, 3, 5(2), ...
3	$A_2^- \oplus T_1^- \oplus T_2^-$	T_1^+	4, 6, 8(2), ...
4	$A_1^+ \oplus E^+ \oplus T_1^+ \oplus T_2^+$	T_2^+	2, 4, 6(2), ...
5	$E^- \oplus 2T_1^- \oplus T_2^-$	T_2^-	3, 5, 7(2), ...
6	$A_1^+ \oplus A_2^+ \oplus E^+ \oplus T_1^+ \oplus 2T_2^+$	E^+	2, 4, 6, ...
		E^-	5, 7, 9, ...
...	...	A_2^-	3, 7, 9, ...
		A_2^+	6, 10, 12, ...

matrix can then be block-diagonalized in the new basis vectors, as illustrated in the following equation,

$$H = \begin{pmatrix} irrep1 & 0 & 0 \\ 0 & irrep2 & 0 \\ 0 & 0 & \ddots \end{pmatrix}. \tag{15}$$

In this manner, the discrete energy spectrum in each irrep sector can be computed separately in a subspace of the Hamiltonian. The separation can be done by group theoretical projection operators. To this end, we need to examine how the group elements of O_h act on our basis states. We first work with the O group which contains the proper rotations, and add the space inversion separately later for the O_h group. We do not need to examine all 24 elements of the O group. In fact, we only to need to focus on two generating elements of the O group which we choose as C_{4z}^+ and C_{4y}^+.

For a rotation $\boldsymbol{r}' = \mathcal{R}\boldsymbol{r}$, the quantum operator on the coordinate-space vectors behaves as $R|\boldsymbol{r}\rangle = |\mathcal{R}\boldsymbol{r}\rangle$. Hence, $\langle\boldsymbol{r}|R^\dagger = \langle\mathcal{R}\boldsymbol{r}|$, and so $\langle\boldsymbol{r}|R = \langle\mathcal{R}^{-1}\boldsymbol{r}|$. For a vector $\boldsymbol{r} = x\hat{\boldsymbol{i}} + y\hat{\boldsymbol{j}} + z\hat{\boldsymbol{k}}$, the action of $(C_{4z}^+)^{-1} = C_{4z}^-$ produces a vector $-x\hat{\boldsymbol{j}} + y\hat{\boldsymbol{i}} + z\hat{\boldsymbol{k}}$. Hence, $(C_{4z}^+)^{-1}|x,y,z\rangle = |y,-x,z\rangle$ and $\langle x,y,z|C_{4z}^+ = \langle y,-x,z|$. Thus, under C_{4z}^+, we have

$$\begin{aligned}\langle x,y,z|C_{4z}^+|n_x,n_y,n_z\rangle &= \langle y,-x,z|n_x,n_y,n_z\rangle = \phi_{n_x}(y)\phi_{n_y}(-x)\phi_{n_z}(z) \\ &= (-1)^{n_y}\phi_{n_y}(x)\phi_{n_x}(y)\phi_{n_z}(z) = (-1)^{n_y}\langle x,y,z|n_y,n_x,n_z\rangle,\end{aligned}$$

from which we conclude

$$\langle n'_x,n'_y,n'_z|C_{4z}^+|n_x,n_y,n_z\rangle = (-1)^{n_y}\delta_{n'_xn_y}\delta_{n'_yn_x}\delta_{n'_zn_z}. \tag{16}$$

Similarly, under C_{4y}^+, we have

$$\begin{aligned}\langle x,y,z|C_{4y}^+|n_x,n_y,n_z\rangle &= \langle -z,y,x|n_x,n_y,n_z\rangle = \phi_{n_x}(-z)\phi_{n_y}(y)\phi_{n_z}(x) \\ &= (-1)^{n_x}\phi_{n_z}(x)\phi_{n_y}(y)\phi_{n_x}(z) = (-1)^{n_x}\langle x,y,z|n_z,n_y,n_x\rangle,\end{aligned}$$

from which we conclude

$$\langle n'_x,n'_y,n'_z|C_{4y}^+|n_x,n_y,n_z\rangle = (-1)^{n_x}\delta_{n'_xn_z}\delta_{n'_yn_y}\delta_{n'_zn_x}. \tag{17}$$

We need to consider three types of basis states separately: all three components are the same, $|n,n,n\rangle$; two components are the same, $|n,n,m\rangle$; all three components are different, $|n,m,k\rangle$. We seek a matrix representation to handle the three types. For the first type, we obtain a 1-dimensional representation of the operations,

$$F[C_{4z}^+] = (-1)^n, F[C_{4y}^+] = (-1)^n. \tag{18}$$

For the second type, if we use 1, 2, 3 to represent the three possibilities $|n,n,m\rangle$, $|n,m,n\rangle$, $|m,n,n\rangle$, respectively, we obtain a three-dimensional matrix

representation of the operations,

$$F[C_{4z}^{+}] = \begin{bmatrix} (-1)^n & 0 & 0 \\ 0 & 0 & (-1)^n \\ 0 & (-1)^m & 0 \end{bmatrix}, \quad F[C_{4y}^{+}] = \begin{bmatrix} 0 & 0 & (-1)^m \\ 0 & (-1)^n & 0 \\ (-1)^n & 0 & 0 \end{bmatrix}. \quad (19)$$

For the third type, if we use 1, 2, 3, 4, 5, 6 to represent the six possibilities $|k,m,n\rangle$, $|k,n,m\rangle$, $|m,k,n\rangle$, $|m,n,k\rangle$, $|n,k,m\rangle$, $|n,m,k\rangle$, respectively, we obtain a six-dimensional matrix representation of the operations,

$$F[C_{4z}^{+}] = \begin{bmatrix} 0 & 0 & (-1)^k & 0 & 0 & 0 \\ 0 & 0 & 0 & 0 & (-1)^k & 0 \\ (-1)^m & 0 & 0 & 0 & 0 & 0 \\ 0 & 0 & 0 & 0 & 0 & (-1)^m \\ 0 & (-1)^n & 0 & 0 & 0 & 0 \\ 0 & 0 & 0 & (-1)^n & 0 & 0 \end{bmatrix},$$

$$F[C_{4y}^{+}] = \begin{bmatrix} 0 & 0 & 0 & 0 & 0 & (-1)^n \\ 0 & 0 & 0 & (-1)^m & 0 & 0 \\ 0 & 0 & 0 & 0 & (-1)^n & 0 \\ 0 & (-1)^k & 0 & 0 & 0 & 0 \\ 0 & 0 & (-1)^m & 0 & 0 & 0 \\ (-1)^k & 0 & 0 & 0 & 0 & 0 \end{bmatrix}. \quad (20)$$

Next, to obtain the other elements, we need the multiplication table for the O group (which can be found in the companion package to save space). The noncommunicative table reflects the closure property that all group elements must satisfy. Inspecting this multiplication table, we can deduce the remaining 22 elements from C_{4z}^{+} and C_{4y}^{+} via a variety of pathways. We choose the following path way (left to right, then down):

$$\begin{array}{llll} C_{2y} = C_{4y}^{+}C_{4y}^{+} \rightarrow & C_{4y}^{-} = C_{2y}C_{4y}^{+} \rightarrow & C_{2z} = C_{4z}^{+}C_{4z}^{+} \rightarrow & C_{4z}^{-} = C_{2z}C_{4z}^{+} \rightarrow \\ C_{34}^{+} = C_{4y}^{+}C_{4z}^{-} \rightarrow & C_{4x}^{-} = C_{4z}^{+}C_{34}^{+} \rightarrow & C_{2x} = C_{4x}^{-}C_{4x}^{-} \rightarrow & C_{4x}^{+} = C_{2x}C_{4x}^{-} \rightarrow \\ C_{31}^{+} = C_{4x}^{+}C_{4y}^{+} \rightarrow & C_{32}^{+} = C_{4y}^{-}C_{4z}^{+} \rightarrow & C_{33}^{+} = C_{4y}^{-}C_{4z}^{-} \rightarrow & C_{31}^{-} = C_{4z}^{-}C_{4y}^{-} \rightarrow \\ C_{32}^{-} = C_{4z}^{-}C_{4y}^{+} \rightarrow & C_{33}^{-} = C_{4z}^{+}C_{4y}^{+} \rightarrow & C_{34}^{-} = C_{4z}^{+}C_{4y}^{-} \rightarrow & C_{2a} = C_{2y}C_{4z}^{+} \rightarrow \\ C_{2b} = C_{2x}C_{4z}^{+} \rightarrow & C_{2c} = C_{4y}^{+}C_{2z} \rightarrow & C_{2d} = C_{2z}C_{4x}^{+} \rightarrow & C_{2e} = C_{2z}C_{4y}^{+} \rightarrow \\ C_{2f} = C_{2y}C_{4x}^{+} \rightarrow & E = C_{2x}C_{2x}. & & \end{array} \quad (21)$$

Formally, the O_h group can be obtained from the O group by the direct product $O_h = O \otimes C_i$ where C_i is the inversion group $C_i = \{E, i_s\}$ where i_s is the space inversion element. Operationally, the elements for the even-parity irreps are obtained by doubly-extending the 24 elements $\{R\}$ to $\{R, R\}$; while elements for the odd-parity irreps are obtained by $\{R, -R\}$. The action of parity $x \rightarrow -x, y \rightarrow -y, z \rightarrow$

$-z$ on our basis states is particularly simple:

$$\begin{aligned}\langle x,y,z|I_s|n_x,n_y,n_z\rangle &= \langle -x,-y,-z|n_x,n_y,n_z\rangle = \phi_{n_x}(-x)\phi_{n_y}(-y)\phi_{n_z}(-z)\\ &= (-1)^{n_x+n_y+n_z}\phi_{n_x}(x)\phi_{n_y}(y)\phi_{n_z}(z)\\ &= (-1)^{n_x+n_y+n_z}\langle x,y,z|n_x,n_y,n_z\rangle, \end{aligned} \tag{22}$$

from which we conclude

$$\langle n'_x,n'_y,n'_z|I_s|n_x,n_y,n_z\rangle = (-1)^{n_x+n_y+n_z}\delta_{n'_x n_x}\delta_{n'_y n_y}\delta_{n'_z n_z}. \tag{23}$$

So we have diagonal representations of dimension 1, 3, and 6, respectively: $F[i_s] = (-1)^{3n} = (-1)^n$ for the first type, $F[i_s] = (-1)^{2n+m} = (-1)^m$ for the second type, and $F[i_s] = (-1)^{k+m+n}$ for the third type. To obtain the matrix representation for the operations in the O_h group, we doubly extend the original operations $F[R]$ with the space inversion applied, $\{F[R], F[i_s]F[R]\}$.

Finally, the basis vectors that transform corresponding to a given row of a given irrep can be found by a projection operator. For any given state $|\varphi\rangle$, a state which resides in row λ of irrep Λ can be obtained by the projection

$$|\Lambda\lambda\rangle = \frac{d_\Lambda}{g}\sum_{R\in\mathcal{G}}\Gamma^{(\Lambda)}_{\lambda\mu}(R)^* U_R|\varphi\rangle, \tag{24}$$

where d_Λ is the dimensionality of the irrep Λ, g is the number of elements in the symmetry group $\mathcal{G}$, Γ is the representation matrix, and U_R is the unitary operator that affects the symmetry operation R on the state. Note that μ is arbitrary. To see this, act with U_G on this state:

$$\begin{aligned} U_G|\Lambda\lambda\rangle &= \frac{d_\Lambda}{g}\sum_{R\in\mathcal{G}}\Gamma^{(\Lambda)}_{\lambda\mu}(R)^* U_G U_R|\varphi\rangle = \frac{d_\Lambda}{g}\sum_{GR\in\mathcal{G}}\Gamma^{(\Lambda)}_{\lambda\mu}(G^{-1}GR)^* U_{GR}|\varphi\rangle\\ &= \Gamma^{(\Lambda)}_{\lambda\nu}(G^{-1})^*|\Lambda\nu\rangle = |\Lambda\nu\rangle\Gamma^{(\Lambda)}_{\nu\lambda}(G). \end{aligned} \tag{25}$$

Hence, for a starting basis of states $|\varphi_n\rangle$, one computes the projection matrix

$$P^\Lambda_\lambda(m,n) = \frac{d_\Lambda}{g}\sum_{R\in\mathcal{G}}\Gamma^{(\Lambda)}_{\lambda\lambda}(R)^* F_{mn}[R], \tag{26}$$

where $F_{mn}[R] = \langle\varphi_m|U_R|\varphi_n\rangle$ denotes the unitary matrix that implements the operation on the Fourier basis for element R. The *columns* of $P^\Lambda_\lambda(m,n)$ show the superposition coefficients in terms of the original basis for the states which reside in row λ of irrep Λ. By taking the transpose, the rows then reveal these superpositions. Different rows give equivalent basis so we work with just one row. The matrix may not be full rank, in which case a QR decomposition can be used to obtain an orthonormal set of independent basis states. The projector $P^\Lambda_\lambda(m,n)$ comes in three types corresponding to the three basis types for the Fourier modes. The basis vectors thus obtained for the O_h group are given in Table 2. The representation matrices $\Gamma^{(\Lambda)}_{\lambda\mu}(R)$ needed to carry out the projection can be found in Table XIII of Ref. 7

Table 2. Orthonormal basis state superpositions that transform according to row 1 of the O_h group in the cubic box. There are three types: all three directions are the same, two the same, and all three different. In all cases, $n \neq m \neq k$ is assumed, and in cases where a state has three different indices, it should be assumed that $k < m < n$. These basis states are used in the block-diagonalization of the Hamiltonian by irreps.

Irrep	Projected Fourier basis states as superposition of $\|n_x n_y n_z\rangle$
A_1^+	$\|n,n,n\rangle$, n even
	$\frac{1}{\sqrt{3}}(\|n,n,m\rangle + \|n,m,n\rangle + \|m,n,n\rangle)$, n,m even
	$\frac{1}{\sqrt{6}}(\|k,m,n\rangle + \|k,n,m\rangle + \|m,k,n\rangle + \|m,n,k\rangle + \|n,k,m\rangle + \|n,m,k\rangle)$, n,m,k even
A_1^-	$\frac{1}{\sqrt{6}}(\|k,m,n\rangle - \|k,n,m\rangle - \|m,k,n\rangle + \|m,n,k\rangle + \|n,k,m\rangle - \|n,m,k\rangle)$, n,m,k odd
A_2^+	$\frac{1}{\sqrt{6}}(\|k,m,n\rangle - \|k,n,m\rangle - \|m,k,n\rangle + \|m,n,k\rangle + \|n,k,m\rangle - \|n,m,k\rangle)$, n,m,k even
A_2^-	$\|n,n,n\rangle$, n odd
	$\frac{1}{\sqrt{3}}(\|n,n,m\rangle + \|n,m,n\rangle + \|m,n,n\rangle)$, n,m odd
	$\frac{1}{\sqrt{6}}(\|k,m,n\rangle + \|k,n,m\rangle + \|m,k,n\rangle + \|m,n,k\rangle + \|n,k,m\rangle + \|n,m,k\rangle)$, n,m,k odd
E^+	$\frac{1}{\sqrt{2}}(\|n,m,n\rangle - \|m,n,n\rangle)$, n,m even
	$\frac{1}{2}(\|k,m,n\rangle + \|k,n,m\rangle - \|m,k,n\rangle - \|n,k,m\rangle)$, n,m,k even
	$\frac{1}{\sqrt{12}}(\|k,m,n\rangle - \|k,n,m\rangle - \|m,k,n\rangle - 2\|m,n,k\rangle + \|n,k,m\rangle + 2\|n,m,k\rangle)$, n,m,k even
E^-	$\frac{1}{\sqrt{6}}(2\|n,n,m\rangle - \|n,m,n\rangle - \|m,n,n\rangle)$, n,m odd
	$\frac{1}{2}(\|k,m,n\rangle - \|k,n,m\rangle + \|m,k,n\rangle - \|n,k,m\rangle)$, n,m,k odd
	$\frac{1}{\sqrt{12}}(\|k,m,n\rangle + \|k,n,m\rangle - \|m,k,n\rangle - 2\|m,n,k\rangle + \|n,k,m\rangle - 2\|n,m,k\rangle)$, n,m,k odd
T_1^+	$\frac{1}{\sqrt{2}}(\|k,m,n\rangle - \|k,n,m\rangle)$, n,m odd, k even
	$\frac{1}{\sqrt{2}}(\|m,k,n\rangle - \|m,n,k\rangle)$, n,k odd, m even
	$\frac{1}{\sqrt{2}}(\|n,k,m\rangle - \|n,m,k\rangle)$, n even, m,k odd
T_1^-	$\|m,n,n\rangle$, n even, m odd
	$\frac{1}{\sqrt{2}}(\|k,m,n\rangle + \|k,n,m\rangle)$, n,m even, k odd
	$\frac{1}{\sqrt{2}}(\|m,k,n\rangle + \|m,n,k\rangle)$, n,k even, m odd
	$\frac{1}{\sqrt{2}}(\|n,k,m\rangle + \|n,m,k\rangle)$, n odd, m,k even
T_2^+	$\|m,n,n\rangle$, n odd, m even
	$\frac{1}{\sqrt{2}}(\|k,m,n\rangle + \|k,n,m\rangle)$, n,m odd, k even
	$\frac{1}{\sqrt{2}}(\|n,k,m\rangle + \|n,m,k\rangle)$, n even, m,k odd
	$\frac{1}{\sqrt{2}}(\|m,k,n\rangle + \|m,n,k\rangle)$, n,k odd, m even
T_2^-	$\frac{1}{\sqrt{2}}(\|k,m,n\rangle - \|k,n,m\rangle)$, n,m even, k odd
	$\frac{1}{\sqrt{2}}(\|m,k,n\rangle - \|m,n,k\rangle)$, n,k even, m odd
	$\frac{1}{\sqrt{2}}(\|n,k,m\rangle - \|n,m,k\rangle)$, n odd, m,k even

(also in the package). A closer inspection of the table reveals the even–odd symmetry pairs in the projected Fourier bases: $A_1^+ \leftrightarrow A_2^-$, $A_1^- \leftrightarrow A_2^+$, $T_1^+ \leftrightarrow T_2^-$, $T_1^- \leftrightarrow T_2^+$, have even and odd switched for all cases of k, m, n. No such obvious symmetry exists between E^+ and E^-. These relations are used as extra checks of the calculations.

In Fig. 4, we show the energy spectrum (lowest 100 levels) as a function of the box size (called a stabilization diagram) for all ten irreps. We use the following criteria for selecting how many projected Fourier basis states in the table (represented by superpositions of $|k,m,n\rangle$) to achieve stable results. For individual Fourier modes,

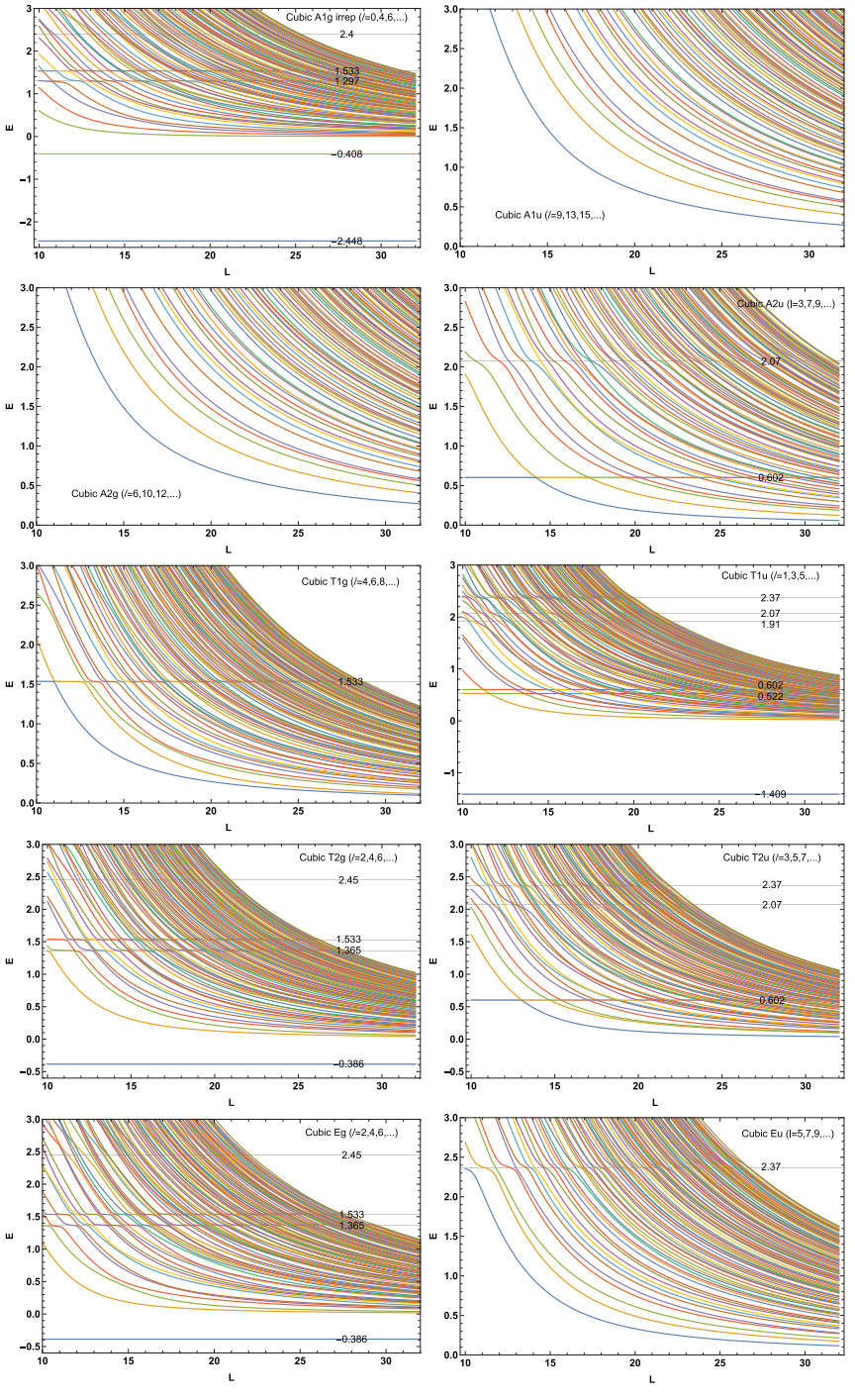

Fig. 4. (Color online) Energy spectrum for the spin-0 system as a function of the cubic box size L for all 10 irreps of the O_h group.

we use up to $k, m, n = 32$. For total Fourier modes, we use up to $k + m + n = 38$. For the damped modes, we used a damping factor $\gamma = 0.5$ with individual damped modes up to 4 and total damped modes up to 4. For example, in the A_1^+ channel, we ended up with four damped basis states (consisting of 10 individual $|n_x n_y n_z\rangle$ modes), and 307 undamped basis vectors (consisting of 1510 individual $|n_x n_y n_z\rangle$ modes). The dimension of the H matrix to be diagonalized is 311. For the other irreps, this size of the H matrix is 146, 146, 235, 504, 374, 605, 707, 705, 609. Typically, it takes about 10 s on my laptop (2014 model Macbook Pro) to obtain all eigenvalues for a fixed box size L; so about 1110 s to do L from 10 to 32 in steps of 0.2, and around 3 h to run all 10 irreps. The bulk of the time is spent on evaluating the Fourier integrals to construct the H matrix. For speed, this part of the computation is outsourced to C++ code, but its execution is handled seamlessly from inside Mathematica.

All the infinite-volume states in Fig. 1 should show up in the 10 irrep sectors. To aid the comparison, faint gridlines are drawn at values expected in the infinite-volume spectrum. The A_1^+ irrep couples to angular momentum $l = 0, 4, 6, \ldots$ (see Table 1). The two $l = 0$ bound states with $E = -2.448$ and $E = -0.409$ are found in this channel. The inclusion of damped modes reduces the need for larger basis vectors to capture the bound states. The bound states have very little dependence on the box size, as one might expect. The $l = 1$ bound state with $E = -1.409$ is found in the T_1^- sector which couples to $l = 1, 3, 5, \ldots$. The last bound state with $l = 2$ and $E = -0.386$ is found in both T_2^+ and E^+ channels which both couple to $l = 2, 4, 6, \ldots$. The parity of a given angular momentum $J = l$ is given by $(-1)^l$ in the spin-0 system.

The scattering states are quantized and the gap between levels is decreasing with increasing box size L, as expected. Resonances reveal themselves in such diagrams as a sequence of avoided level crossings; the closer they approach each other, the sharper the resonance. In the A_1^+ channel, we see clearly two sharp resonances; one at $E = 1.297$ with $l = 0$, and one at $E = 1.533$ with $l = 4$. The next two resonances expected in this channel are broad: one at $E = 2.4$ with $l = 0$, and $E = 2.7$ with $l = 4$. Broad resonances are not as visible as narrow ones in stabilization diagrams. Nonetheless, their properties (pole position and width) can be extracted from a quantitative analysis using Lüscher's method which is beyond the scope of this paper. The next two sectors, A_1^- and A_2^+, are relatively featureless because they couple to higher-partial waves (starting at $l = 9$ and $l = 6$ respectively). The A_2^- channel couples to $l = 3, 7, 9, \ldots$, where the $E = 0.602$ with $l = 3$ state is clearly visible, as well as the slightly broader resonance at $E = 2.07$ with $l = 3$. The T_1^+ channel couples to $l = 4, 6, 8, \ldots$, where the $E = 1.533$ with $l = 4$ state is sitting there alone. This channel is better than the A_1^+ to isolate the $l = 4$ resonance in the system. There is also some hint of the broad $l = 4$ state at $E = 2.70$. The only channel to access p-wave states is the T_1^-. In addition to the sharp $l = 1$ resonance at $E = 0.522$, one finds the close-by $l = 3$ resonance at $E = 0.602$. The lowest $l = 5$ resonance at

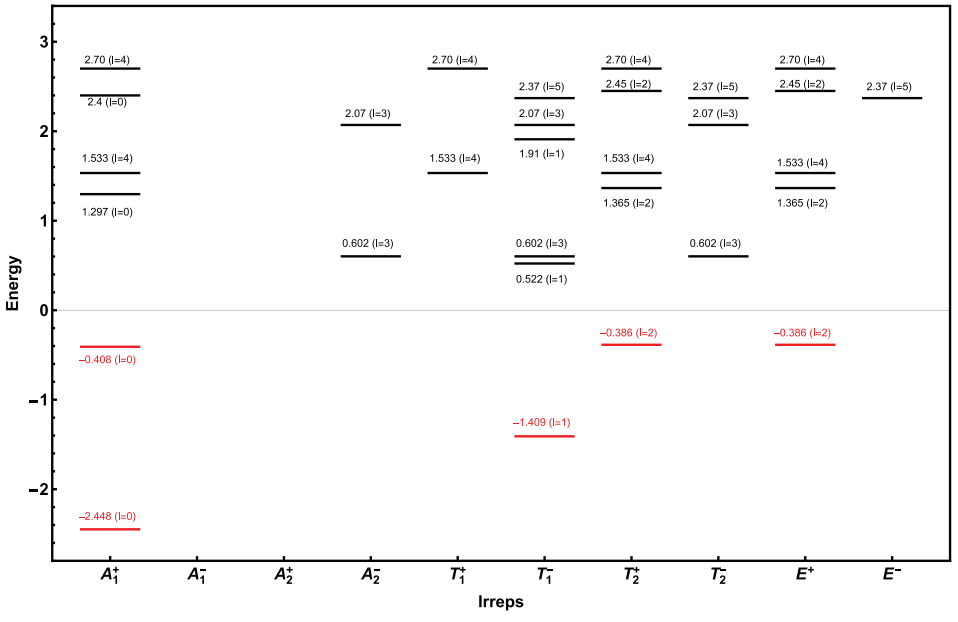

Fig. 5. (Color online) Energy spectrum for the spin-0 system for the 10 irreps of the O_h group in the cubic box, extracted from Fig. 4. It should be compared with Fig. 1. Only states with $E < 3$ and $\ell \leq 5$ are listed.

$E = 2.37$ is also visible, but less so the $l = 1$ state at $E = 1.91$ and the $l = 3$ state at $E = 2.07$. In fact, the best channel to access the $l = 3$ resonance at $E = 0.602$ is T_2^- and A_2^-, and the best channel to access the $l = 5$ resonance at $E = 2.37$ is the E^-. Both are the lowest and well-isolated in these channels. The T_2^+ and E^+ sectors have very similar spectra. They both couple to $l = 2, 4, 6, \ldots$ and have the same bound state and scattering resonances. We summarize the above findings in Fig. 5. It offers a clear overview of how the infinite-volume spectrum in Fig. 1 is resolved in the cubic box.

3.3. *Spin-1/2 system*

For a system of a spinless particle and a spin-1/2 particle in the cubic box, the situation is similar to the spin-0 system in the previous section, except that the matrix elements of the Hamiltonian operator $H = T + V_c + V_{sl}$ are evaluated in a new basis including spin,

$$\begin{aligned}\langle n_x' n_y' n_z', \varepsilon' | H | n_x n_y n_z, \varepsilon \rangle = {} & \delta_{\epsilon'\epsilon} \langle n_x' n_y' n_z' | T | n_x n_y n_z \rangle + \delta_{\epsilon'\epsilon} \langle n_x' n_y' n_z' | V_c | n_x n_y n_z \rangle \\ & + \langle n_x' n_y' n_z', \varepsilon' | V_{s\ell} | n_x n_y n_z, \varepsilon \rangle, \end{aligned} \tag{27}$$

where $|n_x n_y n_z, \varepsilon\rangle$ stands for the Fourier basis coupled to spin-1/2 which is taken as the direct product of the spatial part $|n_x n_y n_z\rangle$ and the spin part $|\varepsilon\rangle$. Here $\varepsilon = +(-)$

refers to "spin-up" and "spin-down" for the spin-1/2 operator s_z. The kinetic energy term T and the spin-independent central potential term V_c can be handled as before; only diagonal terms in spin space survive because of the orthogonality $\langle\epsilon'|\epsilon\rangle = \delta_{\epsilon'\epsilon}$. The spin-orbit term adds off-diagonal elements that require the evaluation of

$$\langle n'_x n'_y n'_z, \varepsilon' | \boldsymbol{s} \cdot \ell | n_x n_y n_z, \varepsilon \rangle = \langle n'_x n'_y n'_z, \varepsilon' | s_x \ell_x + s_y \ell_y + s_z \ell_z | n_x n_y n_z, \varepsilon \rangle. \tag{28}$$

It can be carried out by using the spin operator $\boldsymbol{s} = \sigma/2$ in terms of Pauli spin matrices σ, and the orbital angular momentum operators in Cartesian coordinates (recall we use $\hbar = 1$),

$$\ell_x = -i\left(y\frac{\partial}{\partial z} - z\frac{\partial}{\partial y}\right), \quad \ell_y = -i\left(x\frac{\partial}{\partial z} - z\frac{\partial}{\partial x}\right), \quad \ell_z = -i\left(x\frac{\partial}{\partial y} - y\frac{\partial}{\partial x}\right). \tag{29}$$

Unlike the spin-zero case, the Hamiltonian matrix can be complex-valued due to the complexity both in the operators and the basis vectors to be discussed below.

Since the total angular momentum involves half-integers, we need the double-cover of the O group, denoted as ${}^2O$ which has 48 elements and three additional irreps named G_1, G_2, and H with respective dimensionality of $2, 2, 4$. The full symmetry group including parity is called ${}^2O_h$ which has 96 elements and 16 irreps $A_1^{\pm}$, $A_2^{\pm}$, $E^{\pm}$, $T_1^{\pm}$, $T_2^{\pm}$, $G_1^{\pm}$, $G_2^{\pm}$, and $H^{\pm}$. Full details of the ${}^2O$ group are found in Table XIII of Ref. 7. The six new irreps are responsible for the classification of half-integer angular momentum, as shown in Table 3.

To figure out how the Fourier basis behaves under the ${}^2O_h$ group, we only need to focus on the half-integer irreps G_1, G_2, and H. Parity will be added later as before. To determine the behavior under C_{4z}^+ and C_{4y}^+, first recall that, for spin-$\frac{1}{2}$ states, we have

$$C_{4z}^+ = \frac{1}{\sqrt{2}}\begin{bmatrix} 1-i & 0 \\ 0 & 1+i \end{bmatrix}, \quad C_{4y}^+ = \frac{1}{\sqrt{2}}\begin{bmatrix} 1 & -1 \\ 1 & 1 \end{bmatrix},$$

Table 3. Decomposition of angular momentum in the cubic box according to the six half-integer irreps of the ${}^2O_h$ group. Both the original decomposition (left) and its inverse (right) are shown.

J	${}^2O_h$	${}^2O_h$	J
1/2	$G_1^{\pm}$	$G_1^{\pm}$	1/2, 7/2, 9/2, ...
3/2	$H^{\pm}$	$H^{\pm}$	3/2, 5/2, 7/2, ...
5/2	$G_2^{\pm} \oplus H^{\pm}$	$G_2^{\pm}$	5/2, 7/2, 11/2, ...
7/2	$G_1^{\pm} \oplus G_2^{\pm} \oplus H^{\pm}$		
...	...		

where the states are ordered $|+\rangle, |-\rangle$. Thus, under C_{4z}^+, we have

$$\langle n_x', n_y', n_z'; \varepsilon' | C_{4z}^+ | n_x, n_y, n_z; \varepsilon \rangle$$
$$= (-1)^{n_y} \frac{1}{\sqrt{2}} (1 - i\varepsilon) \delta_{n_x' n_y} \delta_{n_y' n_x} \delta_{n_z' n_z} \delta_{\varepsilon' \varepsilon}, \quad (\varepsilon = \pm 1). \tag{30}$$

Under C_{4y}^+, we have

$$\langle n_x', n_y', n_z'; \varepsilon' | C_{4y}^+ | n_x, n_y, n_z; \varepsilon \rangle = \frac{1}{\sqrt{2}} (-1)^{n_x} \min(1, \varepsilon - \varepsilon' + 1) \delta_{n_x' n_z} \delta_{n_y' n_y} \delta_{n_z' n_x}. \tag{31}$$

There are three types we need to consider: (1) states of the form $|n, n, n; \varepsilon\rangle$; (2) states of the form $|n, n, m; \varepsilon\rangle$, where $n \neq m$; and (3) states of the form $|n, m, k; \varepsilon\rangle$ where $n \neq m \neq k$.

The representation matrices for type 1 are two-dimensional. If we order the states according to $|n, n, n, +\rangle, |n, n, n, -\rangle$, then

$$F[C_{4z}^+] = \frac{(-1)^n}{\sqrt{2}} \begin{bmatrix} 1 - i & 0 \\ 0 & 1 + i \end{bmatrix}, \quad F[C_{4y}^+] = \frac{(-1)^n}{\sqrt{2}} \begin{bmatrix} 1 & -1 \\ 1 & 1 \end{bmatrix}. \tag{32}$$

When n is even, these states reside in the G_{1g} irrep, and when n is odd, these states transform according to the G_{2u} irrep, as we will see later.

The representation matrices for type 2 are six-dimensional. If we choose states 1,2,3 to be, respectively, $|n, n, m, +\rangle, |n, m, n, +\rangle, |m, n, n, +\rangle$, and states 4,5,6 to be, respectively, $|n, n, m, -\rangle, |n, m, n, -\rangle, |m, n, n, -\rangle$, then

$$F[C_{4z}^+] = \frac{1}{\sqrt{2}} \begin{bmatrix} (-1)^n(1-i) & 0 & 0 & 0 & 0 & 0 \\ 0 & 0 & (-1)^n(1-i) & 0 & 0 & 0 \\ 0 & (-1)^m(1-i) & 0 & 0 & 0 & 0 \\ 0 & 0 & 0 & (-1)^n(1+i) & 0 & 0 \\ 0 & 0 & 0 & 0 & 0 & (-1)^n(1+i) \\ 0 & 0 & 0 & 0 & (-1)^m(1+i) & \end{bmatrix}, \tag{33}$$

$$F[C_{4y}^+] = \frac{1}{\sqrt{2}} \begin{bmatrix} 0 & 0 & (-1)^m & 0 & 0 & -(-1)^m \\ 0 & (-1)^n & 0 & 0 & -(-1)^n & 0 \\ (-1)^n & 0 & 0 & -(-1)^n & 0 & 0 \\ 0 & 0 & (-1)^m & 0 & 0 & (-1)^m \\ 0 & (-1)^n & 0 & 0 & (-1)^n & 0 \\ (-1)^n & 0 & 0 & (-1)^n & 0 & 0 \end{bmatrix}. \tag{34}$$

The representation matrices for type 3 are 12-dimensional. Assuming $k < m < n$ and choosing states 1,2,3,4,5,6 to be $|k, m, n, +\rangle, |k, n, m, +\rangle, |m, k, n, +\rangle, |m, n, k, +\rangle, |n, k, m, +\rangle, |n, m, k, +\rangle$, and states 7,8,9,10,11,12 to be $|k, m, n, -\rangle, |k, n, m, -\rangle, |m, k, n, -\rangle, |m, n, k, -\rangle, |n, k, m, -\rangle, |n, m, k, -\rangle$, we have (defining $\alpha = 1 + i$ to

save space)

$$F[C^+_{4z}]=\frac{1}{\sqrt{2}}\begin{bmatrix}
0 & 0 & (-1)^k\alpha^* & 0 & 0 & 0 & 0 & 0 & 0 & 0 & 0 & 0\\
0 & 0 & 0 & 0 & (-1)^k\alpha^* & 0 & 0 & 0 & 0 & 0 & 0 & 0\\
(-1)^m\alpha^* & 0 & 0 & 0 & 0 & 0 & 0 & 0 & 0 & 0 & 0 & 0\\
0 & 0 & 0 & 0 & 0 & (-1)^m\alpha^* & 0 & 0 & 0 & 0 & 0 & 0\\
0 & (-1)^n\alpha^* & 0 & 0 & 0 & 0 & 0 & 0 & 0 & 0 & 0 & 0\\
0 & 0 & 0 & (-1)^n\alpha^* & 0 & 0 & 0 & 0 & 0 & 0 & 0 & 0\\
0 & 0 & 0 & 0 & 0 & 0 & 0 & 0 & (-1)^k\alpha & 0 & 0 & 0\\
0 & 0 & 0 & 0 & 0 & 0 & 0 & 0 & 0 & 0 & (-1)^k\alpha & 0\\
0 & 0 & 0 & 0 & 0 & 0 & (-1)^m\alpha & 0 & 0 & 0 & 0 & 0\\
0 & 0 & 0 & 0 & 0 & 0 & 0 & 0 & 0 & 0 & 0 & (-1)^m\alpha\\
0 & 0 & 0 & 0 & 0 & 0 & 0 & (-1)^n\alpha & 0 & 0 & 0 & 0\\
0 & 0 & 0 & 0 & 0 & 0 & 0 & 0 & 0 & (-1)^n\alpha & 0 & 0
\end{bmatrix}, \tag{35}$$

$$F[C^+_{4y}]=\frac{1}{\sqrt{2}}\begin{bmatrix}
0 & 0 & 0 & 0 & 0 & (-1)^n & 0 & 0 & 0 & 0 & 0 & -(-1)^n\\
0 & 0 & 0 & (-1)^m & 0 & 0 & 0 & 0 & 0 & -(-1)^m & 0 & 0\\
0 & 0 & 0 & 0 & (-1)^n & 0 & 0 & 0 & 0 & 0 & -(-1)^n & 0\\
0 & (-1)^k & 0 & 0 & 0 & 0 & 0 & -(-1)^k & 0 & 0 & 0 & 0\\
0 & 0 & (-1)^m & 0 & 0 & 0 & 0 & 0 & -(-1)^m & 0 & 0 & 0\\
(-1)^k & 0 & 0 & 0 & 0 & 0 & -(-1)^k & 0 & 0 & 0 & 0 & 0\\
0 & 0 & 0 & 0 & 0 & (-1)^n & 0 & 0 & 0 & 0 & 0 & (-1)^n\\
0 & 0 & 0 & (-1)^m & 0 & 0 & 0 & 0 & 0 & (-1)^m & 0 & 0\\
0 & 0 & 0 & 0 & (-1)^n & 0 & 0 & 0 & 0 & 0 & (-1)^n & 0\\
0 & (-1)^k & 0 & 0 & 0 & 0 & 0 & (-1)^k & 0 & 0 & 0 & 0\\
0 & 0 & (-1)^m & 0 & 0 & 0 & 0 & 0 & (-1)^m & 0 & 0 & 0\\
(-1)^k & 0 & 0 & 0 & 0 & 0 & (-1)^k & 0 & 0 & 0 & 0 & 0
\end{bmatrix}. \tag{36}$$

To obtain the remaining 46 elements, we need the multiplication table for the double group ^2O (given in the package). Inspecting this multiplication table, we can deduce the remaining 46 elements from C^+_{4y} and C^+_{4z} via a variety of pathways. We choose the following (left to right, then down):

$$\begin{aligned}
&C_{2y}=C^+_{4y}C^+_{4y}\to \tilde{C}^-_{4y}=C_{2y}C^+_{4y}\to \tilde{E}=\tilde{C}^-_{4y}C^+_{4y}\to \tilde{C}^+_{4y}=\tilde{E}C^+_{4y}\to \tilde{C}_{2y}=\tilde{C}^+_{4y}C^+_{4y}\to\\
&C^-_{4y}=\tilde{C}_{2y}C^+_{4y}\to C_{2z}=C^+_{4z}C^+_{4z}\to \tilde{C}^-_{4z}=C_{2z}C^+_{4z}\to \tilde{C}^+_{4z}=\tilde{E}C^+_{4z}\to \tilde{C}_{2z}=\tilde{C}^+_{4z}C^+_{4z}\to\\
&C^-_{4z}=\tilde{C}_{2z}C^+_{4z}\to C^+_{31}=C^+_{4y}C^+_{4z}\to C^+_{4x}=C^-_{4z}C^+_{31}\to C_{2x}=C^+_{4x}C^+_{4x}\to \tilde{C}^-_{4x}=C_{2x}C^+_{4x}\to\\
&\tilde{C}^+_{4x}=\tilde{E}C^+_{4x}\to \tilde{C}_{2x}=\tilde{C}^+_{4x}C^+_{4x}\to C^-_{4x}=\tilde{C}_{2x}C^+_{4x}\to C^+_{32}=C^-_{4y}C^+_{4z}\to C^+_{34}=C^+_{4y}C^-_{4z}\to\\
&C^+_{33}=C^-_{4y}C^-_{4z}\to C^-_{32}=C^-_{4z}C^+_{4y}\to C^-_{34}=C^+_{4z}C^-_{4y}\to C^-_{33}=C^+_{4z}C^+_{4y}\to C^-_{31}=C^-_{4z}C^-_{4y}\to\\
&C_{2a}=C_{2y}C^+_{4z}\to C_{2b}=\tilde{C}_{2x}C^+_{4z}\to C_{2c}=C^+_{4y}C_{2z}\to C_{2d}=C_{2z}C^+_{4x}\to C_{2e}=C_{2z}C^+_{4y}\to\\
&C_{2f}=C_{2z}C^-_{4x}\to \tilde{C}^+_{31}=\tilde{E}C^+_{31}\to \tilde{C}^+_{32}=\tilde{E}C^+_{32}\to \tilde{C}^+_{33}=\tilde{E}C^+_{33}\to \tilde{C}^+_{34}=\tilde{E}C^+_{34}\to\\
&\tilde{C}^-_{31}=\tilde{E}C^-_{31}\to \tilde{C}^-_{32}=\tilde{E}C^-_{32}\to \tilde{C}^-_{33}=\tilde{E}C^-_{33}\to \tilde{C}^-_{34}=\tilde{E}C^-_{34}\to \tilde{C}_{2a}=\tilde{E}C_{2a}\to\\
&\tilde{C}_{2b}=\tilde{E}C_{2b}\to \tilde{C}_{2c}=\tilde{E}C_{2c}\to \tilde{C}_{2d}=\tilde{E}C_{2d}\to \tilde{C}_{2e}=\tilde{E}C_{2e}\to \tilde{C}_{2f}=\tilde{E}C_{2f}\to E=\tilde{C}_{2x}C_{2x}.
\end{aligned} \tag{37}$$

The 48 elements satisfy the generic double group property that the matrices representing elements C and $\tilde{C}$ differ only by a sign: $F[C]=-F[\tilde{C}]$. This is true for all 24

pairs of the double group in the even-dimensional half-integer irreps (G_1^+, G_2^+, H^+). The property is used here as a consistency check after all the matrices are found. Inclusion of parity is done in the same way as in the single group case. The parity representations are the same $F[i_s] = (-1)^{3n} = (-1)^n$ for the first type, $F[i_s] = (-1)^{2n+m} = (-1)^m$ for the second type, and $F[i_s] = (-1)^{k+m+n}$ for the third type, except multiplied by identity matrix of different dimensions 2, 6, and 12, respectively. The basis vectors obtained for the ${}^2O_h$ group are given in Table 4. The representation matrices $\Gamma^{(\Lambda)}_{\lambda\mu}(R)$ needed to carry out the projection in Eq. (26) can be found in Table XIII of Ref. 7 (also in the package). They correspond to eigenstates of spin harmonics of $|JM\ell\rangle$ with half-integer J and specific values of $\ell = J \pm 1/2$, not

Table 4. Orthonormal basis state superpositions that transform according to row 1 of the double-valued irreps of ${}^2O_h$ in the cubic box. In all cases, $n \neq m \neq k$, and in cases where a state has three different indices, it should be assumed that $k < m < n$. For a given J value, the two l values are $l = J \pm 1/2$, with parity assignment by $(-1)^l$.

Irrep	Projected Fourier basis states as superposition of $\|n_x n_y n_z, \varepsilon\rangle$
G_1^+	$\|n,n,n,+\rangle$, n even
	$\frac{1}{\sqrt{3}}(\|n,n,m,+\rangle + \|n,m,n,+\rangle + \|m,n,n,+\rangle)$, n,m even
	$\frac{1}{\sqrt{6}}(\|k,m,n,+\rangle + \|k,n,m,+\rangle + \|m,k,n,+\rangle + \|m,n,k,+\rangle + \|n,k,m,+\rangle + \|n,m,k,+\rangle)$, k,m,n even
	$\frac{1}{\sqrt{6}}(\|k,m,n,+\rangle - \|m,k,n,+\rangle - i\|k,n,m,-\rangle + i\|m,n,k,-\rangle + \|n,k,m,-\rangle - \|n,m,k,-\rangle)$, k,m odd, n even
	$\frac{1}{\sqrt{6}}(\|k,n,m,+\rangle - \|n,k,m,+\rangle - i\|k,m,n,-\rangle + \|m,k,n,-\rangle - \|m,n,k,-\rangle + i\|n,m,k,-\rangle)$, k,n odd, m even
	$\frac{1}{\sqrt{6}}(\|m,n,k,+\rangle - \|n,m,k,+\rangle + \|k,m,n,-\rangle - \|k,n,m,-\rangle - i\|m,k,n,-\rangle + i\|n,k,m,-\rangle)$, k even, m,n odd
G_1^-	$\frac{1}{\sqrt{3}}(\|n,n,m,+\rangle + i\|n,m,n,-\rangle + \|m,n,n,-\rangle)$, n even, m odd
	$\frac{1}{\sqrt{6}}(\|k,m,n,+\rangle - \|k,n,m,+\rangle - \|m,k,n,+\rangle + \|m,n,k,+\rangle + \|n,k,m,+\rangle - \|n,m,k,+\rangle)$, k,m,n odd
	$\frac{1}{\sqrt{6}}(\|k,m,n,+\rangle + \|m,k,n,+\rangle + i\|k,n,m,-\rangle + i\|m,n,k,-\rangle + \|n,k,m,-\rangle + \|n,m,k,-\rangle)$, k,m even, n odd
	$\frac{1}{\sqrt{6}}(\|k,n,m,+\rangle + \|n,k,m,+\rangle + i\|k,m,n,-\rangle + \|m,k,n,-\rangle + \|m,n,k,-\rangle + i\|n,m,k,-\rangle)$, k,n even, m odd
	$\frac{1}{\sqrt{6}}(\|m,n,k,+\rangle + \|n,m,k,+\rangle + \|k,m,n,-\rangle + \|k,n,m,-\rangle + i\|m,k,n,-\rangle + i\|n,k,m,-\rangle)$, k odd, m,n even
G_2^+	$\frac{1}{\sqrt{3}}(\|n,n,m,+\rangle + i\|n,m,n,-\rangle + \|m,n,n,-\rangle)$, n odd, m even
	$\frac{1}{\sqrt{6}}(\|k,m,n,+\rangle - \|k,n,m,+\rangle - \|m,k,n,+\rangle + \|m,n,k,+\rangle + \|n,k,m,+\rangle - \|n,m,k,+\rangle)$, k,m,n even
	$\frac{1}{\sqrt{6}}(\|k,m,n,+\rangle + \|m,k,n,+\rangle + i\|k,n,m,-\rangle + i\|m,n,k,-\rangle + \|n,k,m,-\rangle + \|n,m,k,-\rangle)$, k,m odd, n even
	$\frac{1}{\sqrt{6}}(\|k,n,m,+\rangle + \|n,k,m,+\rangle + i\|k,m,n,-\rangle + \|m,k,n,-\rangle + \|m,n,k,-\rangle + i\|n,m,k,-\rangle)$, k,n odd, m even
	$\frac{1}{\sqrt{6}}(\|m,n,k,+\rangle + \|n,m,k,+\rangle + \|k,m,n,-\rangle + \|k,n,m,-\rangle + i\|m,k,n,-\rangle + i\|n,k,m,-\rangle)$, k even, m,n odd
G_2^-	$\|n,n,n,+\rangle$, n odd
	$\frac{1}{\sqrt{3}}(\|n,n,m,+\rangle + \|n,m,n,+\rangle + \|m,n,n,+\rangle)$, n,m odd
	$\frac{1}{\sqrt{6}}(\|k,m,n,+\rangle + \|k,n,m,+\rangle + \|m,k,n,+\rangle + \|m,n,k,+\rangle + \|n,k,m,+\rangle + \|n,m,k,+\rangle)$, k,m,n odd
	$\frac{1}{\sqrt{6}}(\|k,m,n,+\rangle - \|m,k,n,+\rangle - i\|k,n,m,-\rangle + i\|m,n,k,-\rangle + \|n,k,m,-\rangle - \|n,m,k,-\rangle)$, k,m even, n
	$\frac{1}{\sqrt{6}}(\|k,n,m,+\rangle - \|n,k,m,+\rangle - i\|k,m,n,-\rangle + \|m,k,n,-\rangle - \|m,n,k,-\rangle + i\|n,m,k,-\rangle)$, k,n even, m odd
	$\frac{1}{\sqrt{6}}(\|m,n,k,+\rangle - \|n,m,k,+\rangle + \|k,m,n,-\rangle - \|k,n,m,-\rangle - i\|m,k,n,-\rangle + i\|n,k,m,-\rangle)$, k odd, m,n even
H^+	$\frac{1}{\sqrt{6}}(\|n,m,n,+\rangle + i\|m,n,n,+\rangle + 2i\|n,n,m,-\rangle)$, n odd, m even
	$\frac{1}{\sqrt{2}}(\|n,m,n,-\rangle - \|m,n,n,-\rangle)$, n,m even
	$\frac{1}{\sqrt{12}}(2\|k,m,n,-\rangle + \|k,n,m,-\rangle - 2\|m,k,n,-\rangle - \|m,n,k,-\rangle - \|n,k,m,-\rangle + \|n,m,k,-\rangle)$, k,m,n even
	$\frac{1}{2}(\|k,n,m,-\rangle + \|m,n,k,-\rangle - \|n,k,m,-\rangle - \|n,m,k,-\rangle)$, k,m,n even
	$\frac{1}{\sqrt{12}}(2\|k,n,m,+\rangle - \|m,n,k,+\rangle + 2i\|n,k,m,+\rangle - i\|n,m,k,+\rangle + i\|k,m,n,-\rangle + i\|m,k,n,-\rangle)$, k,m odd, n even
	$\frac{1}{2}(\|m,n,k,+\rangle + i\|n,m,k,+\rangle + i\|k,m,n,-\rangle + i\|m,k,n,-\rangle)$, k,m odd, n even

Table 4. (*Continued*)

Irrep	Projected Fourier basis states as superposition of $\|n_x n_y n_z, \varepsilon\rangle$
	$\frac{1}{\sqrt{12}}(2\|k,m,n,+\rangle + 2i\|m,k,n,+\rangle - i\|m,n,k,+\rangle - \|n,m,k,+\rangle + i\|k,n,m,-\rangle + i\|n,k,m,-\rangle)$, k,n odd, m even
	$\frac{1}{2}(\|m,n,k,+\rangle - i\|n,m,k,+\rangle + \|k,n,m,-\rangle + \|n,k,m,-\rangle)$, k,n odd, m even
	$\frac{1}{\sqrt{12}}(2\|k,m,n,+\rangle - \|k,n,m,+\rangle - 2i\|m,k,n,+\rangle + i\|n,k,m,+\rangle + \|m,n,k,-\rangle + \|n,m,k,-\rangle)$, k even, m,n odd
	$\frac{1}{2}(\|k,n,m,+\rangle - i\|n,k,m,+\rangle + \|m,n,k,-\rangle + \|n,m,k,-\rangle)$, k even, m,n odd
H^-	$\frac{1}{\sqrt{6}}(2\|n,n,m,-\rangle - \|n,m,n,-\rangle - \|m,n,n,-\rangle)$, n,m odd
	$\frac{1}{2}(\|n,m,n,+\rangle - i\|m,n,n,+\rangle)$, n even, m odd
	$\frac{1}{\sqrt{12}}(2\|k,m,n,-\rangle - \|k,n,m,-\rangle + 2\|m,k,n,-\rangle - \|m,n,k,-\rangle - \|n,k,m,-\rangle - \|n,m,k,-\rangle)$, k,m,n odd
	$\frac{1}{2}(\|k,n,m,-\rangle - \|m,n,k,-\rangle + \|n,k,m,-\rangle - \|n,m,k,-\rangle)$, k,m,n odd
	$\frac{1}{\sqrt{12}}(2\|k,n,m,+\rangle + \|m,n,k,+\rangle - 2i\|n,k,m,+\rangle - i\|n,m,k,+\rangle - i\|k,m,n,-\rangle + i\|m,k,n,-\rangle)$, k,m even, n odd
	$\frac{1}{2}(\|m,n,k,+\rangle - i\|n,m,k,+\rangle + i\|k,m,n,-\rangle - i\|m,k,n,-\rangle)$, k,m even, n odd
	$\frac{1}{\sqrt{12}}(2\|k,m,n,+\rangle - 2i\|m,k,n,+\rangle - i\|m,n,k,+\rangle + \|n,m,k,+\rangle - i\|k,n,m,-\rangle + i\|n,k,m,-\rangle)$, k,n even, m odd
	$\frac{1}{2}(\|m,n,k,+\rangle + i\|n,m,k,+\rangle - \|k,n,m,-\rangle + \|n,k,m,-\rangle)$, k,n even, m odd
	$\frac{1}{\sqrt{12}}(2\|k,m,n,+\rangle + \|k,n,m,+\rangle + 2i\|m,k,n,+\rangle + i\|n,k,m,+\rangle + \|m,n,k,-\rangle - \|n,m,k,-\rangle)$, k odd, m,n even
	$\frac{1}{2}(\|k,n,m,+\rangle + i\|n,k,m,+\rangle - \|m,n,k,-\rangle + \|n,m,k,-\rangle)$, k odd, m,n even

the standard spherical harmonics $|JM\rangle$ with integer $J = \ell$. A closer inspection of the table reveals that the even–odd parity symmetry in the irreps leads to symmetric pairs in the projected Fourier bases: $G_1^+ \leftrightarrow G_2^-$ and $G_1^- \leftrightarrow G_2^+$ have even and odd switched for all cases of k, m, n. No such obvious symmetry exists between $H^+ \leftrightarrow H^-$. These relations are used as additional checks of the calculations.

In Fig. 6, we show the stabilization diagrams (100 low-lying levels) for the spin-1/2 system for the six half-integer irreps of the ${}^2O_h$ group. The results are obtained by the same criteria for selecting the projected Fourier basis states, namely, up to 32 for individual Fourier modes, and up to 38 for total Fourier modes. The same damping parameters are used: $\gamma = 0.5$ with individual damped modes up to 4 and total damped modes up to 4. The resulting basis size (H matrix size) is 916, 853, 906, 844, 1814, and 1690. For the G-type irreps, it takes about 30 s to obtain all eigenvalues for a fixed box size L; so about 3330 seconds to do L from 10 to 32 in steps of 0.2, and about 3.7 hours to run the four irreps. The H-type irreps have larger basis and takes 3 times longer: 90 s instead of 30, or 2.8 h per irrep. The total time for the spin-1/2 system is about 9.3 h, more than triple the timing for the spin-0 system. This is after a performance speed-up by building the Fourier basis directly inside the C++ code. In practice, one does not need the full stabilization diagrams. Often just a few box sizes are sufficient, which is on the order of minutes.

The situation in the spin-1/2 system is more complicated as indicated in the infinite-volume spectrum in Fig. 2. For a given partial wave l, there are two possibilities for the total angular momentum, $J = l + 1/2$ and $J = l - 1/2$, color-coded as blue and red, respectively. The parity of a state is given by $(-1)^l$. Nonetheless, these states are expected to manifest themselves in the six irrep sectors in Fig. 6. Again, to help with the identification, faint gray gridlines are drawn at values expected from the infinite-volume spectrum.

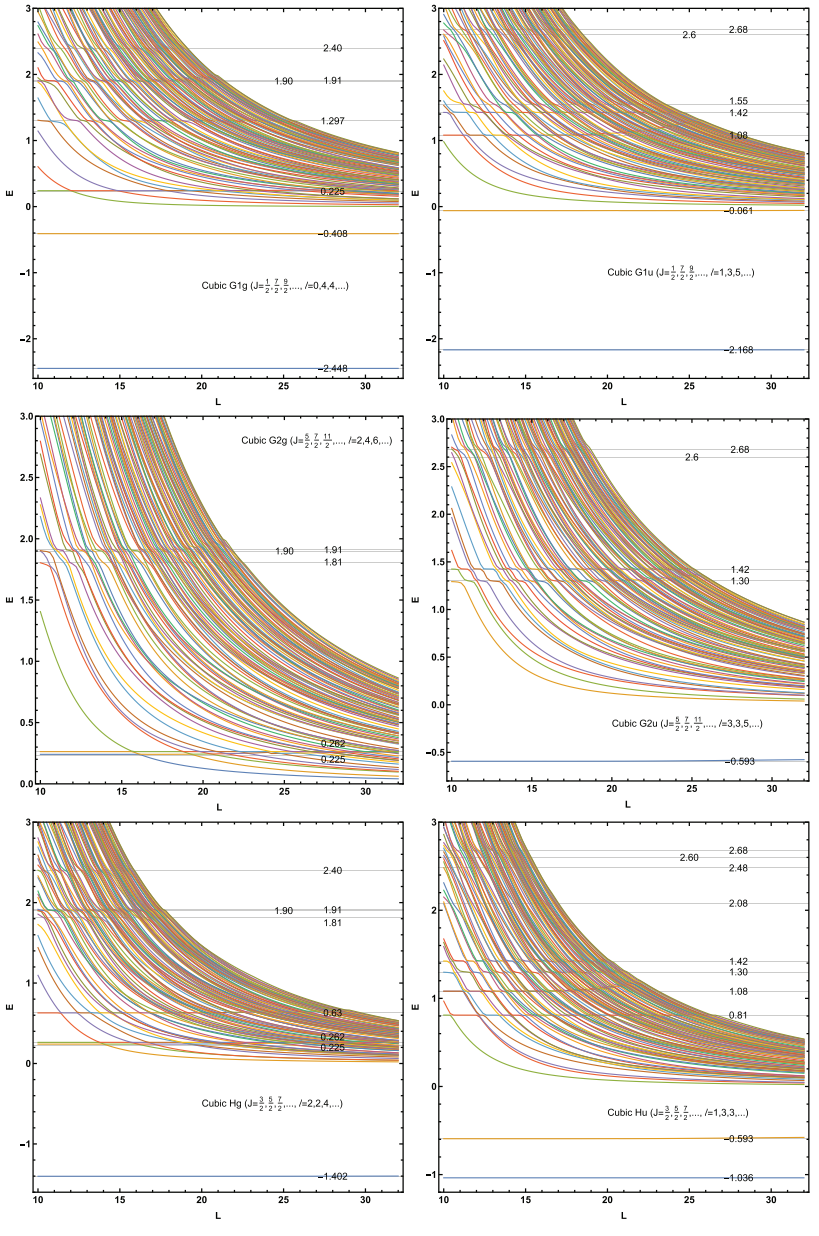

Fig. 6. (Color online) Energy spectrum for the spin-1/2 system as a function of cubic box size L for the six half-integer irreps of the ${}^2O_h$ group. Faint black lines are drawn to guide the eye.

All seven bound states in the spin-1/2 system can be located. Grouped by parity as implied by $(-1)^l$, the G_1^+ channel has the two $J = 1/2, l = 0$ states at $E = -2.448$ and at $E = -0.409$. The H^+ channel has the $J = 3/2, l = 2$ state at $E = -1.402$. For odd parity, the G_1^- channel has the two $J = 1/2, l = 1$ states: one at

$E = -2.168$, the other barely bound at $E = -0.061$. The $J = 5/2, l = 3$ state at $E = -0.593$ is found in both G_2^- and H^-. The remaining $J = 3/2, l = 1$ state at $E = -1.036$ appears in H^-.

The lowest-energy scattering state $E = 0.225$ has high-spin and even-parity $J = 7/2, l = 4$. It appears in all three even-parity channels: it sits alone in G_1^+, but has a close neighbor at $E = 0.262$ and $J = 5/2, l = 2$ in G_1^+ and H^+. The next even-parity state $E = 0.63$ and $J = 3/2, l = 2$ is found in H^+. The lowest-spin resonance with $E = 1.297$ and $J = 1/2, l = 0$ is G_1^+. There are two high-spin states with almost the same energy: one with $E = 1.91$ and $J = 7/2, l = 4$, the other $E = 1.90$ and $J = 11/2, l = 6$ with higher spin but narrower. They are expected in all three even-parity channels are very hard to disentangle. The relatively narrow resonance with $E = 2.4$ and $J = 9/2, l = 4$ is expected in G_1^+ and H^+, but not in G_2^+ because it does not couple to $J = 9/2$. Indeed, this is confirmed in the diagrams.

In the odd-parity channel G_1^-, the lowest-energy resonance at $E = 1.08$ has a high spin $J = 9/2, l = 5$. Since the state is fairly sharp, we can see some divergence for box size larger than 20. It suggests the need for a larger basis for this state. Similar divergence is observed in the H^- where the same state appears. The lowest-spin resonance with $E = 1.55$ and $J = 1/2, l = 1$ is found in G_1^- but it appears as the third resonance in energy. The sharp resonance with $E = 0.81$ and $J = 3/2, l = 1$ appears only in H^- because G_1^- and G_2^- do not couple to $J = 3/2$. The sharp resonance with $E = 1.30$ and $J = 5/2, l = 3$ appears only in G_2^- and H^- but not in

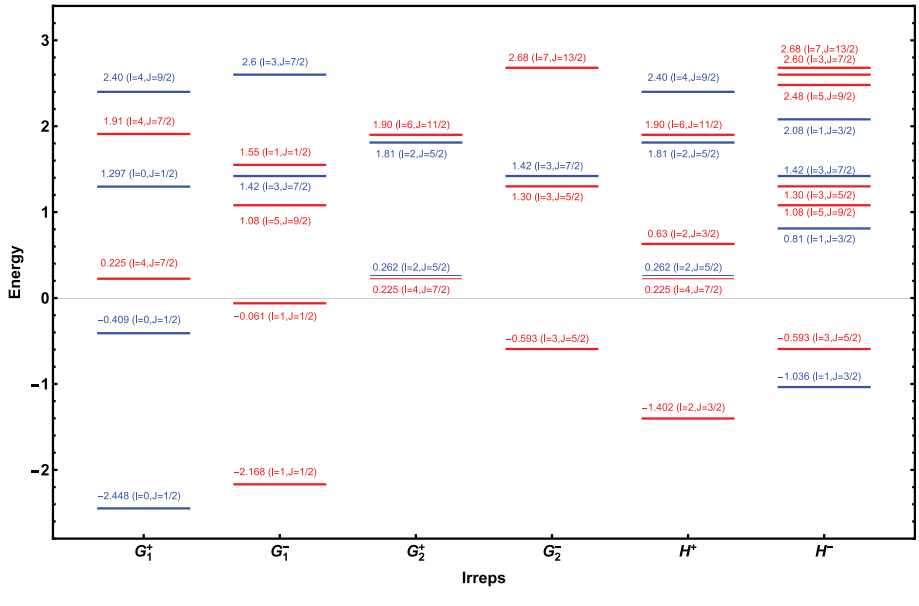

Fig. 7. (Color online) Bound and scattering states for the spin-1/2 system as a function of six half-integer irreps of the ${}^2O_h$ group in the cubic box, extracted from Fig. 6. It should be compared with Fig. 2. Only states with $E < 3$ and $\ell \leq 5$ are listed. For a given partial wave ℓ, there are two possible J values, $J = \ell + 1/2$ (blue) and $J = \ell + 1/2$ (red).

G_1^- because it does not couple to $J = 5/2$. The sharp resonance with $E = 1.42$ and $J = 7/2, l = 3$ appears clearly in all three odd-parity channels. The broad resonance with $E = 2.48$ and $J = 9/2, l = 5$ is expected in G_1^- and H^- but not in G_2^- because it does not couple to $J = 9/2$, but is not very visible in the diagrams due to its broadness. Even higher up, the broad state $E = 2.6$ at $J = 7/2, l = 3$ and relatively narrow state $E = 2.68$ at $J = 13/2, l = 7$ are expected in three odd-parity channels, and are indeed hinted.

The above discussions are summarized in Fig. 7. It can be directly compared with Fig. 2 to see how the infinite-volume spectrum in the spin-1/2 system is resolved in the cubic box.

4. Spectrum in Elongated Box

Here we want to explore the possibility of resolving the same spectrum in an asymmetric box. Compared to the cubic box, two new issues come into play. First, the Fourier integrals need to be treated differently for different directions. This is relatively straightforward. Second, a new symmetry group is required corresponding to the new geometry. A new group means new irreps; hence new decompositions of angular momentum. It also means that new basis projections must be worked out.

4.1. *Spin-0 system*

We consider an elongated box $L \times L \times \eta L$ where η is the elongation factor in the z-direction. The equation we need to solve takes the same form as Eq. (8), but with a modified periodic boundary condition,

$$\psi(x + n_x L, y + n_y L, z + n_z L\eta) = \psi(x, y, z), \tag{38}$$

and a modified potential,

$$V_L(x, y, z) = \sum_{n_x, n_y, n_z} V(|(x + n_x L, y + n_y L, z + n_z L\eta)|). \tag{39}$$

Instead of being rotationally invariant, the potential takes on the symmetry of the elongated box.

The Fourier basis in which the Hamiltonian can be diagonalized receives a modification in the z-component:

$$\langle x, y, z | n_x n_y n_z \rangle = \phi_{n_x}(x, L)\phi_{n_y}(y, L)\phi_{n_z}(z, \eta L). \tag{40}$$

The Hamiltonian matrix elements now depend on both L and η,

$$\begin{aligned}\langle n_x' n_y' n_z' | \hat{H} | n_x n_y n_z \rangle = & \int_{-L/2}^{L/2} dx \int_{-L/2}^{L/2} dy \int_{-\eta L/2}^{\eta L/2} dz\, \phi_{n_x'}(x, L)\phi_{n_y'}(y, L)\phi_{n_z'}(z, \eta L) \\ & \times \hat{H}\phi_{n_x}(x, L)\phi_{n_y}(y, L)\phi_{n_z}(z, \eta L).\end{aligned} \tag{41}$$

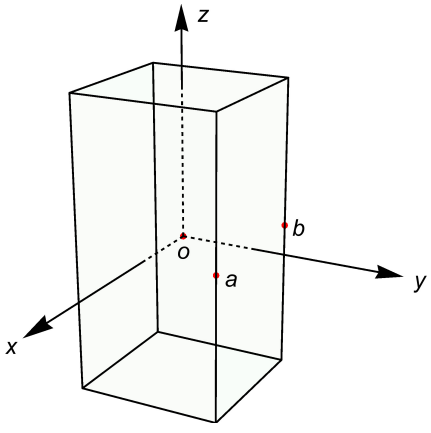

Fig. 8. This box is elongated in the z direction. It is invariant under 8 rotations as explained in the text.

Going from cubic box to elongated box, the symmetry group is reduced from the O group to the D_4 group (dihedral or tetragonal group). It is regarded as a subgroup of the O group. The O and D_4 groups are different finite point groups of the continuous rotation group $SO(3)$. The D_4 group has eight elements instead of 24 in the O group, as depicted in Fig. 8. They can be divided into five conjugacy classes and given names: the identity (E), two $\pi/2$ rotations about z axes ($C_{4z}^{\pm}$); three π rotations about the Cartesian axes (C_{2x},C_{2x},C_{2z}); and two π rotations about the two diagonals in the xy-plane denoted by Oa and Ob (C_{2a}, C_{2b}). The D_4 group has five irreps conventionally named A_1, A_2, B_1, B_2, and E, with respective dimensions 1, 1, 1, 1, 2. Inclusion of parity extends it to the D_{4h} group which has 10 irreps $A_1^{\pm}$, $A_2^{\pm}$, $B_1^{\pm}$, $B_2^{\pm}$, $E^{\pm}$. They are responsible for the decomposition of integer angular momentum in the elongated box, as shown in Table 5. Notice how differently it resolves the angular momentum from that in the cubic box in Table 1.

The Fourier basis vectors that transform according to the irreps of the D_{4h} can be constructed by group theoretical projection operators, in similar fashion to the

Table 5. Decomposition of integer angular momentum in the elongated box according to the 10 irreps of the D_{4h} group.

J	D_{4h}	D_{4h}	J
0	A_1^+	A_1^+	0, 2, 4(2), ...
1	$A_2^- \oplus E^-$	A_1^-	5, 7, 9(2), ...
2	$A_1^+ \oplus B_1^+ \oplus B_2^+ \oplus E^+$	A_2^-	1, 3, 5(2), ...
3	$A_2^- \oplus B_1^- \oplus B_2^- \oplus 2E^-$	A_2^+	4, 6, 8(2), ...
4	$2A_1^+ \oplus A_2^+ \oplus B_1^+ \oplus B_2^+ \oplus 2E^+$	B_1^+	2, 4, 6(2), ...
5	$A_1^- \oplus 2A_2^- \oplus B_1^- \oplus B_2^- \oplus 3E^-$	B_1^-	3, 5, 7(2), ...
6	$2A_1^+ \oplus A_2^+ \oplus 2B_1^+ \oplus 2B_2^+ \oplus 3E^+$	B_2^+	2, 4, 6(2), ...
		B_2^-	3, 5, 7(2), ...
...	...	E^-	1, 3(2), 5(3), ...
		E^+	2, 4(2), 6(3), ...

cubic case. We first work with the D_4 group which contains the proper rotations; then add the space inversion separately to obtain the D_{4h}. We focus on two generating elements of the D_4 group: the $\pi/2$ rotation about the z axis, denoted by C_{4z}^+; and the π rotation about the y axis, denoted by C_{2y}. The action of C_{4z}^+ is the same as in the cubic case. The action of C_{2y}, which rotates the vector $(x, y, z) \to (-x, y, -z)$, gives

$$\langle n'_x, n'_y, n'_z | C_{2y} | n_x, n_y, n_z \rangle = (-1)^{n_x+n_z} \delta_{n'_x n_x} \delta_{n'_y n_y} \delta_{n'_z n_z}. \tag{42}$$

Since the order of x, y, z is preserved by this operation, the matrix representation for the three types of Fourier basis is diagonal. For the first type where all three components are the same, $|n, n, n\rangle$, we simply obtain the identity,

$$F[C_{2y}] = (-1)^{n+n} = 1. \tag{43}$$

For the second type where two components can be different, with 1, 2, 3 representing $|n, n, m\rangle$, $|n, m, n\rangle$, $|m, n, n\rangle$, respectively, we obtain the three-dimensional representation,

$$F[C_{2y}] = \begin{bmatrix} (-1)^{n+m} & 0 & 0 \\ 0 & 1 & 0 \\ 0 & 0 & (-1)^{n+m} \end{bmatrix}. \tag{44}$$

For the third type where all three components are different, with 1, 2, 3, 4, 5, 6 representing $|k, m, n\rangle$, $|k, n, m\rangle$, $|m, k, n\rangle$, $|m, n, k\rangle$, $|n, k, m\rangle$, $|n, m, k\rangle$, respectively, we obtain a six-dimensional representation,

$$F[C_{2y}] = \begin{bmatrix} (-1)^{k+n} & 0 & 0 & 0 & 0 & 0 \\ 0 & (-1)^{k+m} & 0 & 0 & 0 & 0 \\ 0 & 0 & (-1)^{m+n} & 0 & 0 & 0 \\ 0 & 0 & 0 & (-1)^{m+k} & 0 & 0 \\ 0 & 0 & 0 & 0 & (-1)^{n+m} & 0 \\ 0 & 0 & 0 & 0 & 0 & (-1)^{n+k} \end{bmatrix}. \tag{45}$$

The remaining six elements can be obtained by the multiplication table for the D_4 group (given in the package) One possible pathway is:

$$\begin{aligned} C_{2z} = C_{4z}^+ C_{4z}^+ \to C_{4z}^- = C_{4z}^+ C_{2z} \to C_{2a} = C_{4z}^- C_{2y} \to C_{2b} = C_{4z}^+ C_{2y} \to C_{2x} \\ = C_{4z}^+ C_{2b} \to E = C_{2a} C_{2a}. \end{aligned} \tag{46}$$

The diagonal representations are as before: $F[i_s] = (-1)^{3n} = (-1)^n$ for the first type, $F[i_s] = (-1)^{2n+m} = (-1)^m$ for the second type, and $F[i_s] = (-1)^{k+m+n}$ for the third type, multiplied by identity matrix of dimension 1, 3, and 6, respectively. Finally, to obtain the matrix representation for the operations in the D_{4h} group, we doubly extend the original operations $F[R]$ with the space inversion applied, $\{F[R], F[i_s]F[R]\}$. Applying the projection operator in Eq. (26) to the elongated box, we obtain the Fourier basis vectors that transform according to the irreps of the D_{4h} group, given in Table 6. The representation matrices $\Gamma_{\lambda\mu}^{(\Lambda)}(R)$ needed to carry out the

Table 6. Orthonormal basis state superpositions that transform according to row 1 of the D_{4h} group in the elongated box. In all cases, $n \neq m \neq k$, and in cases where a state has three different indices, it should be assumed that $k < m < n$.

Irrep	Projected Fourier basis states as superposition of $\|n_x n_y n_z\rangle$
A_1^+	$\|n,n,n\rangle$, n even
	$\|n,n,m\rangle, \frac{1}{\sqrt{2}}(\|n,m,n\rangle + \|m,n,n\rangle)$, m,n even
	$\frac{1}{\sqrt{2}}(\|k,m,n\rangle + \|m,k,n\rangle)$, k,m,n even
	$\frac{1}{\sqrt{2}}(\|k,n,m\rangle + \|n,k,m\rangle)$, k,m,n even
	$\frac{1}{\sqrt{2}}(\|m,n,k\rangle + \|n,m,k\rangle)$, k,m,n even
A_1^-	$\frac{1}{\sqrt{2}}(\|n,m,n\rangle - \|m,n,n\rangle)$, m,n odd
	$\frac{1}{\sqrt{2}}(\|k,m,n\rangle - \|m,k,n\rangle)$, k,m,n odd
	$\frac{1}{\sqrt{2}}(\|k,n,m\rangle - \|n,k,m\rangle)$, k,m,n odd
	$\frac{1}{\sqrt{2}}(\|m,n,k\rangle - \|n,m,k\rangle)$, k,m,n odd
A_2^+	$\frac{1}{\sqrt{2}}(\|k,m,n\rangle - \|m,k,n\rangle)$, n even, k,m odd
	$\frac{1}{\sqrt{2}}(\|k,n,m\rangle - \|n,k,m\rangle)$, m even, k,n odd
	$\frac{1}{\sqrt{2}}(\|m,n,k\rangle - \|n,m,k\rangle)$, k even, m,n odd
A_2^-	$\|n,n,m\rangle$, m odd, n even
	$\frac{1}{\sqrt{2}}(\|k,m,n\rangle + \|m,k,n\rangle)$, n odd, k,m even
	$\frac{1}{\sqrt{2}}(\|k,n,m\rangle + \|n,k,m\rangle)$, m odd, k,n even
	$\frac{1}{\sqrt{2}}(\|m,n,k\rangle + \|n,m,k\rangle)$, k odd, m,n even
B_1^+	$\frac{1}{\sqrt{2}}(\|n,m,n\rangle - \|m,n,n\rangle)$, m,n even
	$\frac{1}{\sqrt{2}}(\|k,m,n\rangle - \|m,k,n\rangle)$, k,m,n even
	$\frac{1}{\sqrt{2}}(\|k,n,m\rangle - \|n,k,m\rangle)$, k,m,n even
	$\frac{1}{\sqrt{2}}(\|m,n,k\rangle - \|n,m,k\rangle)$, k,m,n even
B_1^-	$\|n,n,n\rangle$, n odd
	$\|n,n,m\rangle, \frac{1}{\sqrt{2}}(\|n,m,n\rangle + \|m,n,n\rangle)$, m,n odd
	$\frac{1}{\sqrt{2}}(\|k,m,n\rangle + \|m,k,n\rangle)$, k,m,n odd
	$\frac{1}{\sqrt{2}}(\|k,n,m\rangle + \|n,k,m\rangle)$, k,m,n odd
	$\frac{1}{\sqrt{2}}(\|m,n,k\rangle + \|n,m,k\rangle)$, k,m,n odd
B_2^+	$\|n,n,m\rangle$, m even, n odd
	$\frac{1}{\sqrt{2}}(\|k,m,n\rangle + \|m,k,n\rangle)$, n even, m,k odd
	$\frac{1}{\sqrt{2}}(\|k,n,m\rangle + \|n,k,m\rangle)$, m even, n,k odd
	$\frac{1}{\sqrt{2}}(\|m,n,k\rangle + \|n,m,k\rangle)$, k even, m,n odd
B_2^-	$\frac{1}{\sqrt{2}}(\|k,m,n\rangle - \|m,k,n\rangle)$, n odd, m,k even
	$\frac{1}{\sqrt{2}}(\|k,n,m\rangle - \|n,k,m\rangle)$, m odd, n,k even
	$\frac{1}{\sqrt{2}}(\|m,n,k\rangle - \|n,m,k\rangle)$, k odd, m,n even
E^+	$\|m,n,n\rangle$, m even, n odd
	$\|k,m,n\rangle, \|k,n,m\rangle$, k even, m,n odd
	$\|m,k,n\rangle, \|m,n,k\rangle$, m even, n,k odd
	$\|n,k,m\rangle, \|n,m,k\rangle$, n even, m,k odd

Table 6. (*Continued*)

Irrep	Projected Fourier basis states as superposition of $\|n_x n_y n_z\rangle$
E^-	$\|m,n,n\rangle$, m odd, n even
	$\|k,m,n\rangle, \|k,n,m\rangle$, k odd, m,n even
	$\|m,k,n\rangle, \|m,n,k\rangle$, m odd, n,k even
	$\|n,k,m\rangle, \|n,m,k\rangle$, n odd, m,k even

projection in Eq. (26) can be found in Table X of Ref. 7. A closer look of the table reveals that the even–odd parity symmetry in the irreps leads to symmetric pairs in the projected Fourier bases. The following pairs have even and odd switched for all cases of k,m,n: $A_1^+ \leftrightarrow B_1^-$, $A_1^- \leftrightarrow B_1^+$, $A_2^+ \leftrightarrow B_2^-$, $A_2^- \leftrightarrow B_2^+$, and $E^+ \leftrightarrow E^-$. These relations are used as additional checks of the calculations.

In Fig. 9, we show the energy spectrum (lowest 100 levels) as a function of the elongation factor η at a fixed box size $L = 12$ for all 10 irreps of the D_{4h} group. The same criteria are used: up to 32 for individual Fourier modes, and 38 for total Fourier modes, as well as the damped modes (damping factor $\gamma = 0.5$ with individual damped modes up to 4 and total damped modes up to 4). The size of the projected Fourier basis (size of H matrix) is 815, 520, 605, 707, 705, 609, 705, 609, 1310, 1316 for the 10 irreps. Typically, it takes about 15 s to obtain all eigenvalues for a fixed value of η; so about 915 s to do η from 0.9 to 2.1 in steps of 0.2, and about 3 h to run all 10 irreps. The code is structured the same way as in the cubic case. The timing is also similar. Even though only one dimension is varied, as opposed to all three dimensions, it is still a single adjustable parameter, η instead of L, that enters the calculations.

How is the same infinite-volume spectrum in Fig. 1 resolved in the elongated box? The first feature to notice is that the "stabilization diagrams" have a different look compared to the cubic case. There are avoided level crossings induced by the elongation, which makes the visual identification of resonances more difficult because it relies on avoided crossings. Second, the spectrum depends on two parameters L and η. One has the freedom to pick a box size L, then vary η. Since the gap between levels is shrinking with increasing L, if a large L is picked, then the levels are more compacted. For this reason, $L = 12$ is picked in the figure where the gap between levels is still relatively large. Note, however, that this does not mean that the elongated box is less effective than the cubic one in resolving states. It is only a matter of visual identification in stabilization diagrams. As far as quantitative phaseshift analysis of the spectrum via the Lüscher method is concerned, the two are not fundamentally different. The elongated geometry does have one advantage when the box is discretized into a periodic lattice as in lattice QCD, where changing one dimension is much cheaper than changing 3 dimensions. Third, the angular momentum resolution is different from that in the cubic case. There are not large gaps between partial waves as in the cubic case. They are relatively spread out across the irreps. This means the same state can appear in multiple irreps more frequently.

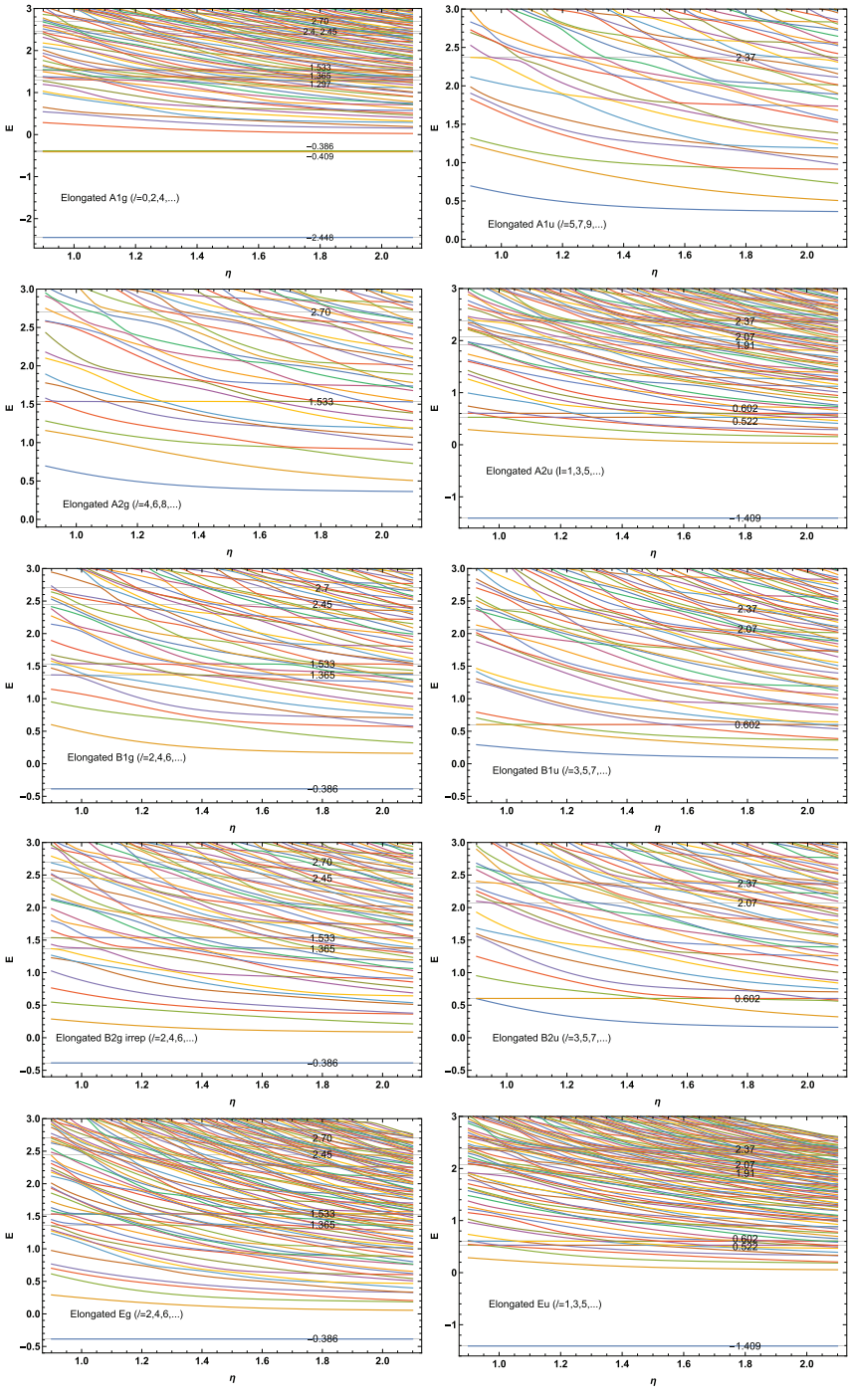

Fig. 9. (Color online) Energy spectrum for the spin-0 system as a function of the elongation factor η for all 10 irreps of the D_{4h} group. The volume of the elongated box is $L \times L \times \eta L$ with $L = 12$.

For bound states, the identification is just as easy as in the cubic case. They have negative values and are expected to be independent of the elongation factor η. In the A_1^+ channel, which couples to angular momentum $l = 0, 2, 4, \ldots$, three bounds are found. The two $l = 0$ states with $E = -2.448$ and $E = -0.409$, and one $l = 2$ state with $E = -0.386$ which also appears in B_1^+, B_2^+, and E^+. The remaining bound state at $E = -1.409$ and $l = 1$ is found in A_2^- and E^-, both of which couple to $l = 1, 3, 5, \ldots$.

For scattering states, only extremely sharp resonances are visible. It is helpful to examine a zoomed-up view of the diagrams. We see the narrow $l = 4$ resonance at $E = 1.533$ is clearly present in the A_2^+ channel, whereas the broad state expected at $E = 2.7$ in the same channel is not. The same $E = 1.533$ state is present in all five even-parity channels because they all couple to $l = 4$. The $l = 2$ resonance at $E = 1.365$ is present in all even-parity channels, except for A_2^+ which it does not couple. The relatively narrow and high-spin $l = 5$ resonance at $E = 2.37$ is present all odd-parity channels. The $l = 3$ resonance at $E = 0.602$ appears in all odd-parity channels, except for A_1^-. The same is true for the $l = 3$ resonance at $E = 2.07$, but is much less clear due to its broadness. The $l = 1$ resonance at $E = 0.522$ appears in A_2^- and E^-. Even though it is very close to the $E = 0.602$ state, it is still distinguishable from each other.

We summarize the above discussions in Fig. 10, which offers a direct comparison with the infinite-volume spectrum in Fig. 1 and the cubic spectrum in Fig. 5.

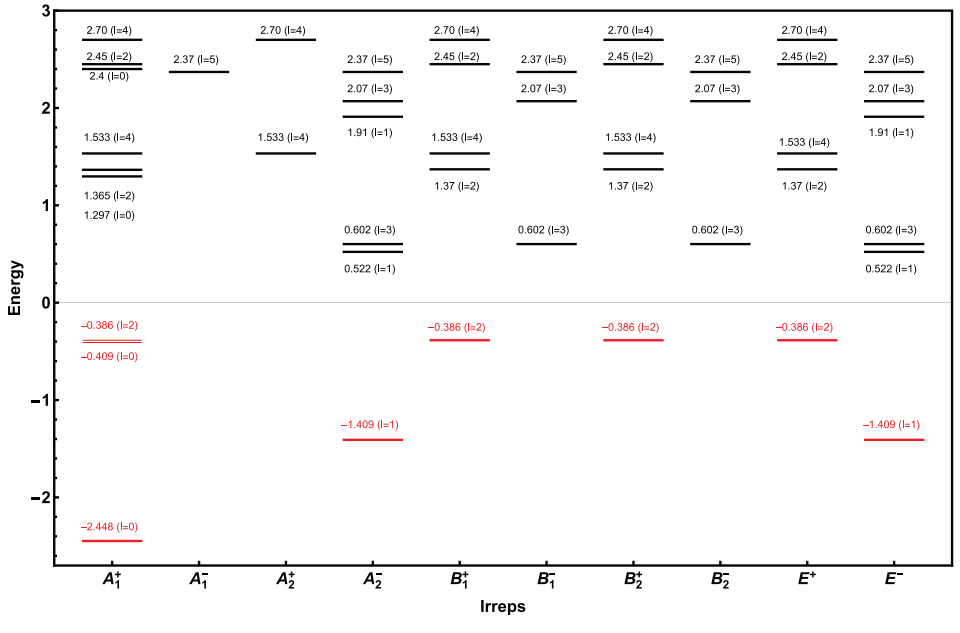

Fig. 10. (Color online) Bound states and resonances for the spin-0 system as a function of the D_{4h} irreps in the elongated box of $L \times L \times \eta L$ at a fixed $L = 12$. Only states with $E < 3$ and $l \leq 6$ are listed. They are extracted from Fig. 9 and should be compared with the infinite-volume spectrum in Fig. 1 and the cubic spectrum in Fig. 5.

4.2. *Spin-1/2 system*

Since the total angular momentum involves half-integers, we need ${}^2D_4$, the double cover group of D_4. The ${}^2D_4$ group has 16 elements and two additional irreps named G_1, G_2 with respective dimensionality of $2, 2$. The ${}^2D_4$ group is discussed in detail in Ref. 7. The full symmetry group including parity is called ${}^2D_{4h}$ which has 32 elements and 14 irreps $A_1^{\pm}$, $A_2^{\pm}$, $B_1^{\pm}$, $B_2^{\pm}$, $E^{\pm}$, $G_1^{\pm}$, and $G_2^{\pm}$. The four new irreps $G_1^{\pm}$, and $G_2^{\pm}$ are responsible for the classification of half-integer angular momentum, as shown in Table 7.

To figure out how the Fourier basis behaves under the ${}^2D_{4h}$ group, we only need to focus on the irreps G_1, G_2 of the ${}^2D_4$ group. Parity will be added later. To determine the behavior under C_{4z}^+ and C_{2y} spin-$\frac{1}{2}$ states, we need their matrix representation in the G_1 irrep, which can be obtained from spin-1/2 rotations $e^{-i\vec{n}\cdot\vec{\sigma}\omega/2}$ (where $\vec{n}$ is unit rotation axis and ω the rotation angle),

$$C_{4z}^+ = \frac{1 - i\sigma_z}{\sqrt{2}} = \frac{1}{\sqrt{2}} \begin{bmatrix} 1-i & 0 \\ 0 & 1+i \end{bmatrix}, \quad C_{2y} = -i\sigma_y = \begin{bmatrix} 0 & -1 \\ 1 & 0 \end{bmatrix},$$

where the states are ordered $|+\rangle, |-\rangle$. Compared to the cubic case (${}^2O$ group), C_{4z}^+ is the same, along with the corresponding unitary matrices $F_{mn}[C_{4z}^+]$; but C_{2y} replaces C_{4y}^+ as the new generator. Under C_{2y}, we have

$$\langle n_x', n_y', n_z'; \varepsilon' | C_{2y} | n_x, n_y, n_z; \varepsilon \rangle = (-1)^{n_x+n_z} \frac{\varepsilon - \varepsilon'}{2} \delta_{n_x' n_x} \delta_{n_y' n_y} \delta_{n_z' n_z}, \tag{47}$$

where the spatial part is diagonal as in the integer-spin case. The representation matrices for type 1 are two-dimensional. If we order the states according to $|n, n, n, +\rangle, |n, n, n, -\rangle$, then

$$F[C_{2y}] = \begin{bmatrix} 0 & -1 \\ 1 & 0 \end{bmatrix}. \tag{48}$$

The representation matrices for type 2 are six-dimensional. If we choose states 1,2,3 to be, respectively, $|n, n, m, +\rangle, |n, m, n, +\rangle, |m, n, n, +\rangle$, and states 4,5,6 to be,

Table 7. Decomposition of angular momentum in the elongated box according to the four half-integer irreps of the ${}^2D_{4h}$ group. Both the original decomposition (left) and its inverse (right) are shown.

J	${}^2D_{4h}$	${}^2D_{4h}$	J
1/2	$G_1^{\pm}$	$G_1^{\pm}$	1/2, 3/2, 5/2, ...
3/2	$G_1^{\pm} \oplus G_2^{\pm}$	$G_2^{\pm}$	3/2, 5/2(2), 7/2(2), ...
5/2	$G_1^{\pm} \oplus 2G_2^{\pm}$		
7/2	$2G_1^{\pm} \oplus 2G_2^{\pm}$		
...	...		

respectively, $|n,n,m,-\rangle, |n,m,n,-\rangle, |m,n,n,-\rangle$, then

$$F[C_{2y}] = \begin{bmatrix} 0 & 0 & 0 & -(-1)^{n+m} & 0 & 0 \\ 0 & 0 & 0 & 0 & -1 & 0 \\ 0 & 0 & 0 & 0 & 0 & -(-1)^{m+n} \\ (-1)^{n+m} & 0 & 0 & 0 & 0 & 0 \\ 0 & 1 & 0 & 0 & 0 & 0 \\ 0 & 0 & (-1)^{m+n} & 0 & 0 & 0 \end{bmatrix}. \tag{49}$$

The representation matrices for type 3 are 12-dimensional. Assuming $k < m < n$ and choosing states 1,2,3,4,5,6 to be $|k,m,n,+\rangle, |k,n,m,+\rangle, |m,k,n,+\rangle, |m,n,k,+\rangle, |n,k,m,+\rangle$, and $|n,m,k,+\rangle$, and states 7,8,9,10,11,12 to be $|k,m,n,-\rangle, |k,n,m,-\rangle, |m,k,n,-\rangle, |m,n,k,-\rangle, |n,k,m,-\rangle, |n,m,k,-\rangle$, we have

$$F[C_{2y}] = \begin{bmatrix} 0 & 0 & 0 & 0 & 0 & 0 & -(-1)^{k+n} & 0 & 0 & 0 & 0 & 0 \\ 0 & 0 & 0 & 0 & 0 & 0 & 0 & -(-1)^{k+m} & 0 & 0 & 0 & 0 \\ 0 & 0 & 0 & 0 & 0 & 0 & 0 & 0 & -(-1)^{m+n} & 0 & 0 & 0 \\ 0 & 0 & 0 & 0 & 0 & 0 & 0 & 0 & 0 & -(-1)^{m+k} & 0 & 0 \\ 0 & 0 & 0 & 0 & 0 & 0 & 0 & 0 & 0 & 0 & -(-1)^{n+m} & 0 \\ 0 & 0 & 0 & 0 & 0 & 0 & 0 & 0 & 0 & 0 & 0 & -(-1)^{n+k} \\ (-1)^{k+n} & 0 & 0 & 0 & 0 & 0 & 0 & 0 & 0 & 0 & 0 & 0 \\ 0 & (-1)^{k+m} & 0 & 0 & 0 & 0 & 0 & 0 & 0 & 0 & 0 & 0 \\ 0 & 0 & (-1)^{m+n} & 0 & 0 & 0 & 0 & 0 & 0 & 0 & 0 & 0 \\ 0 & 0 & 0 & (-1)^{m+k} & 0 & 0 & 0 & 0 & 0 & 0 & 0 & 0 \\ 0 & 0 & 0 & 0 & (-1)^{n+m} & 0 & 0 & 0 & 0 & 0 & 0 & 0 \\ 0 & 0 & 0 & 0 & 0 & (-1)^{n+k} & 0 & 0 & 0 & 0 & 0 & 0 \end{bmatrix}. \tag{50}$$

To obtain the other elements, we need the multiplication table for the double group ${}^2D_4$ (given in the package). Inspecting this multiplication table, we can deduce the remaining 14 elements from C_{2y} and C_{4z}^+ via a variety of pathways. We choose the following:

$$C_{2z} = C_{4z}^+ C_{4z}^+ \to C_{2x} = C_{2y} C_{2z} \to C_{2a} = C_{4z}^+ C_{2x} \to C_{2b} = C_{4z}^+ C_{2y} \to C_{4z}^- = C_{2b} C_{2x} \to$$
$$\tilde{C}_{4z}^+ = C_{2b} C_{2y} \to \tilde{C}_{4z}^- = C_{2z} C_{4z}^+ \to \tilde{C}_{2z} = C_{4z}^- C_{4z}^- \to \tilde{C}_{2x} = C_{4z}^+ C_{2b} \to \tilde{C}_{2y} = C_{2x} C_{2z} \to$$
$$\tilde{C}_{2a} = C_{2z} C_{2b} \to \tilde{C}_{2b} = C_{2x} C_{4z}^+ \to \tilde{E} = C_{2x} C_{2x} \to E = C_{4z}^+ C_{4z}^-. \tag{51}$$

The 16 elements satisfy the generic double group property that the matrices representing elements C and $\tilde{C}$ differ only by a sign: $F[C] = -F[\tilde{C}]$. This is true for all eight pairs of the double group in the half-integer irreps (G_1 and G_2). The property is used here as a consistency check after all the matrices are found. Inclusion of parity is done in the same way as in the single group case. The parity representations are the same $F[i_s] = (-1)^{3n} = (-1)^n$ for the first type, $F[i_s] = (-1)^{2n+m} = (-1)^m$ for the second type, and $F[i_s] = (-1)^{k+m+n}$ for the third type, except multiplied by identity matrix of different dimensions 2, 6, and 12, respectively. The basis vectors obtained for the ${}^2D_{4h}$ group are given in Table 8. Inspection of the table reveals further

Table 8. Orthonormal basis state superpositions that transform according to row 1 of the double-valued irreps of ${}^2D_{4h}$ in the elongated box. In all cases, $n \neq m \neq k$, and in cases where a state has three different indices, it should be assumed that $k < m < n$. For a given J value, the two l values are $l = J \pm 1/2$, with parity assignment by $(-1)^l$.

Irrep	Projected Fourier basis states as superposition of $\|n_x n_y n_z, \varepsilon\rangle$
G_1^+	$\|n,n,n,+\rangle$, n even
	$\|n,n,m,+\rangle, \frac{1}{\sqrt{2}}(\|n,m,n,+\rangle + \|m,n,n,+\rangle)$, m,n even
	$\frac{1}{\sqrt{2}}(\|n,m,n,-\rangle + i\|m,n,n,-\rangle)$, n odd, m even
	$\frac{1}{\sqrt{2}}(\|k,m,n,+\rangle + \|m,k,n,+\rangle), \frac{1}{\sqrt{2}}(\|k,n,m,+\rangle + \|n,k,m,+\rangle), \frac{1}{\sqrt{2}}(\|m,n,k,+\rangle + \|n,m,k,+\rangle)$, k,m,n even
	$\frac{1}{\sqrt{2}}(\|k,m,n,+\rangle - \|m,k,n,+\rangle), \frac{1}{\sqrt{2}}(\|k,n,m,-\rangle + i\|n,k,m,-\rangle), \frac{1}{\sqrt{2}}(\|m,n,k,-\rangle + i\|n,m,k,-\rangle)$, n even, k,m odd
	$\frac{1}{\sqrt{2}}(\|k,n,m,+\rangle - \|n,k,m,+\rangle), \frac{1}{\sqrt{2}}(\|k,m,n,-\rangle + i\|m,k,n,-\rangle), \frac{1}{\sqrt{2}}(\|m,n,k,-\rangle - i\|n,m,k,-\rangle)$, m even, k,n odd
	$\frac{1}{\sqrt{2}}(\|m,n,k,+\rangle - \|n,m,k,+\rangle), \frac{1}{\sqrt{2}}(\|k,m,n,-\rangle - i\|m,k,n,-\rangle), \frac{1}{\sqrt{2}}(\|k,n,m,-\rangle - i\|n,k,m,-\rangle)$, k even, m,n odd
G_1^-	$\|n,n,m,+\rangle, \frac{1}{\sqrt{2}}(\|n,m,n,-\rangle - i\|m,n,n,-\rangle)$, m odd, n even
	$\frac{1}{\sqrt{2}}(\|n,m,n,+\rangle - \|m,n,n,+\rangle)$, m,n odd
	$\frac{1}{\sqrt{2}}(\|k,m,n,+\rangle - \|m,k,n,+\rangle), \frac{1}{\sqrt{2}}(\|k,n,m,+\rangle - \|n,k,m,+\rangle), \frac{1}{\sqrt{2}}(\|m,n,k,+\rangle - \|n,m,k,+\rangle)$, k,m,n odd
	$\frac{1}{\sqrt{2}}(\|k,n,m,+\rangle + \|n,k,m,+\rangle), \frac{1}{\sqrt{2}}(\|k,m,n,-\rangle - i\|m,k,n,-\rangle), \frac{1}{\sqrt{2}}(\|m,n,k,-\rangle + i\|n,m,k,-\rangle)$, m odd, k,n even
	$\frac{1}{\sqrt{2}}(\|k,m,n,+\rangle + \|m,k,n,+\rangle), \frac{1}{\sqrt{2}}(\|k,n,m,-\rangle - i\|n,k,m,-\rangle), \frac{1}{\sqrt{2}}(\|m,n,k,-\rangle - i\|n,m,k,-\rangle)$, n odd, k,m even
	$\frac{1}{\sqrt{2}}(\|m,n,k,+\rangle + \|n,m,k,+\rangle), \frac{1}{\sqrt{2}}(\|k,m,n,-\rangle + i\|m,k,n,-\rangle), \frac{1}{\sqrt{2}}(\|k,n,m,-\rangle + i\|n,k,m,-\rangle)$, k odd, m,n even
G_2^+	$\|n,n,m,+\rangle, \frac{1}{\sqrt{2}}(\|n,m,n,-\rangle - i\|m,n,n,-\rangle)$, m even, n odd
	$\frac{1}{\sqrt{2}}(\|n,m,n,+\rangle - \|m,n,n,+\rangle)$, m,n even
	$\frac{1}{\sqrt{2}}(\|k,m,n,+\rangle - \|m,k,n,+\rangle), \frac{1}{\sqrt{2}}(\|k,n,m,+\rangle - \|n,k,m,+\rangle), \frac{1}{\sqrt{2}}(\|m,n,k,+\rangle - \|n,m,k,+\rangle)$, k,m,n even
	$\frac{1}{\sqrt{2}}(\|k,n,m,+\rangle + \|n,k,m,+\rangle), \frac{1}{\sqrt{2}}(\|k,m,n,-\rangle - i\|m,k,n,-\rangle), \frac{1}{\sqrt{2}}(\|m,n,k,-\rangle + i\|n,m,k,-\rangle)$, m even, k,n odd
	$\frac{1}{\sqrt{2}}(\|k,m,n,+\rangle + \|m,k,n,+\rangle), \frac{1}{\sqrt{2}}(\|k,n,m,-\rangle - i\|n,k,m,-\rangle), \frac{1}{\sqrt{2}}(\|m,n,k,-\rangle - i\|n,m,k,-\rangle)$, n even, k,m odd
	$\frac{1}{\sqrt{2}}(\|m,n,k,+\rangle + \|n,m,k,+\rangle), \frac{1}{\sqrt{2}}(\|k,m,n,-\rangle + i\|m,k,n,-\rangle), \frac{1}{\sqrt{2}}(\|k,n,m,-\rangle + i\|n,k,m,-\rangle)$, k even, m,n odd
G_2^-	$\|n,n,n,+\rangle$, n odd
	$\|n,n,m,+\rangle, \frac{1}{\sqrt{2}}(\|n,m,n,+\rangle + \|m,n,n,+\rangle)$, m,n odd
	$\frac{1}{\sqrt{2}}(\|n,m,n,-\rangle + i\|m,n,n,-\rangle)$, n even, m odd
	$\frac{1}{\sqrt{2}}(\|k,m,n,+\rangle + \|m,k,n,+\rangle), \frac{1}{\sqrt{2}}(\|k,n,m,+\rangle + \|n,k,m,+\rangle), \frac{1}{\sqrt{2}}(\|m,n,k,+\rangle + \|n,m,k,+\rangle)$, k,m,n odd
	$\frac{1}{\sqrt{2}}(\|k,m,n,+\rangle - \|m,k,n,+\rangle), \frac{1}{\sqrt{2}}(\|k,n,m,-\rangle + i\|n,k,m,-\rangle), \frac{1}{\sqrt{2}}(\|m,n,k,-\rangle + i\|n,m,k,-\rangle)$, n odd, k,m even
	$\frac{1}{\sqrt{2}}(\|k,n,m,+\rangle - \|n,k,m,+\rangle), \frac{1}{\sqrt{2}}(\|k,m,n,-\rangle + i\|m,k,n,-\rangle), \frac{1}{\sqrt{2}}(\|m,n,k,-\rangle - i\|n,m,k,-\rangle)$, m odd, k,n even
	$\frac{1}{\sqrt{2}}(\|m,n,k,+\rangle - \|n,m,k,+\rangle), \frac{1}{\sqrt{2}}(\|k,m,n,-\rangle - i\|m,k,n,-\rangle), \frac{1}{\sqrt{2}}(\|k,n,m,-\rangle - i\|n,k,m,-\rangle)$, k odd, m,n even

symmetries. The G_1^+ and G_2^- have even and odd switched for all cases of k, m, n. Same is true between G_1^- and G_2^+. These symmetry properties serve as additional checks of the calculations.

In Fig. 9, we show the energy spectrum (lowest 100 levels) as a function of the elongation factor η at a fixed box size $L = 12$ for all ten irreps of the D_{4h} group. For the normal Fourier modes, we used the criteria of up to 26 for individual modes, and 28 for total modes. For the damped Fourier modes, we used damping factor $\gamma = 0.5$ with individual modes up to 4 and total modes up to 4, except for the G_2^- channel where $\gamma = 0.6$ and 5 were used. This is done to better capture the bound states. The size of the projected Fourier basis (size of H matrix) is 1191, 1076, 1182, 1079 for the four irreps. Typically, it takes about 15 s to obtain all eigenvalues for a fixed value of

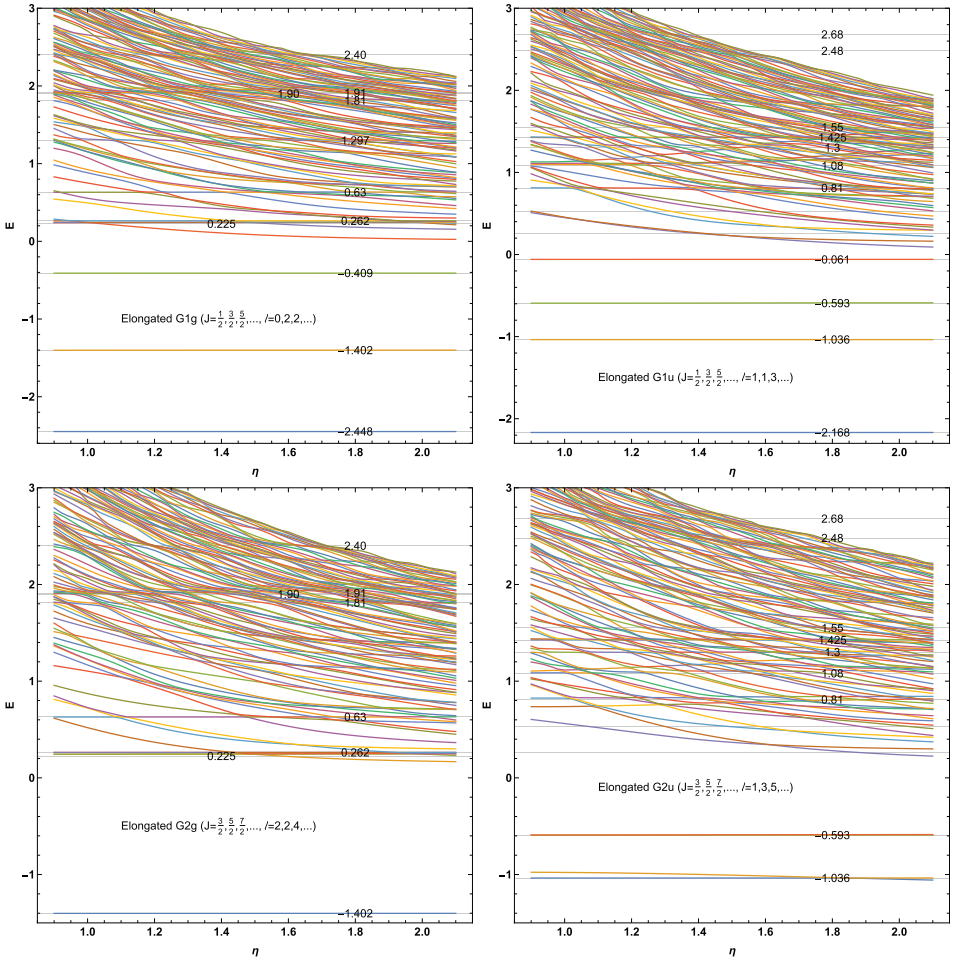

Fig. 11. (Color online) Stabilization diagrams for the spin-1/2 system from the four half-integer irreps of the ${}^2D_{4h}$ group in the elongated box of $L \times L \times \eta L$ with $L = 12$.

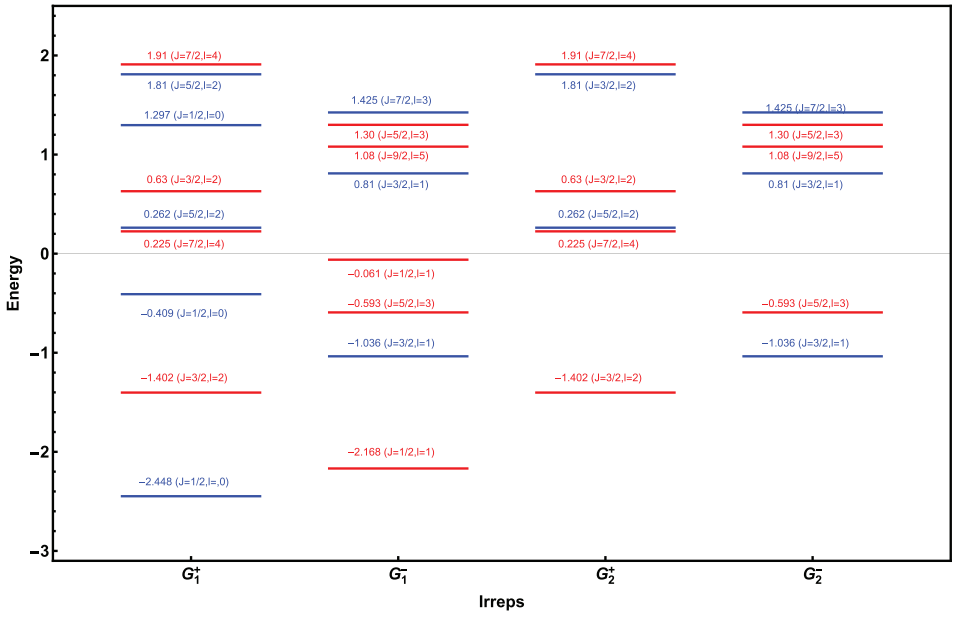

Fig. 12. (Color online) Energy spectrum of the spin-1/2 system in the elongated box of $L = 12$ as a function of η for the half-integer irreps of the ${}^2D_{4h}$ group. They are extracted from Fig. 11 and should be compared with the infinite-volume spectrum in Fig. 2 and the cubic spectrum in Fig. 7.

η; so about 915 s to do η from 0.9 to 2.1 in steps of 0.2, and about an hour to run all four irreps. The code is structured the same way as in the cubic case for the spin-1/2 system, but takes much less time (1 h vs. 9 h). One obvious factor is we have four irreps in the elongated box as opposed to six irreps in the cubic box. The more important factor is in the structure of the projected Fourier basis. In the cubic case (see Table 4), most of the states are superposition of six individual modes, whereas in the elongated case (see Table 8), the states are superposition of two individual modes. This is especially true of the four-dimensional $H^{\pm}$ irreps in the cubic case. As a result, more individual modes are used in the cubic case.

For bound states, all seven are identified in the four diagrams. In the even-parity G_1^+ channel, which couples to total angular momentum $J = 1/2, 3/2, 5/2, \ldots$, we see the two $J = 1/2$ states with $E = -2.448$ and $E = -0.409$, and the one $J = 3/2$ state with $E = -1.402$ which also appears in G_2^+. In the odd-parity G_1^- channel, which couples to the same total angular momentum, we see four bound states: the two $J = 1/2$ states with $E = -2.168$ and $E = -0.061$, the $J = 3/2$ state with $E = -1.036$, and the $J = 5/2$ state with $E = -0.593$. The $E = -0.593$ and $E = -1.036$ also appear in the G_2^- channel as doubly degenerate states.

For scattering states, the visual identification is more difficult; only extremely sharp resonances are visible. The three low-lying even-parity resonances $E = 0.225$, $E = 0.262$, and $E = 0.63$ are found in both G_1^+ and G_2^+. The $E = 1.297$ state is in G_1^+ but not in G_2^+ because the latter does not couple to $J = 1/2$. The three high-lying

even-parity resonances $E = 1.81$, $E = 1.90$, $E = 1.91$, and $E = 2.40$ also appear in both channels. In the odd-parity channels, the sharp states at $E = 0.81$, $E = 1.08$, $E = 1.3$, and $E = 1.45$ are visible, whereas the broad ones at $E = 1.55$, $2.08, 2.48, 2.6, 2.68$ are less so.

The final outcome for the spin-1/2 system in the elongated box is summarized in Fig. 10 along with assigned quantum numbers. It offers a direct comparison with the infinite-volume spectrum in Fig. 2 and the cubic spectrum in Fig. 7.

5. Summary and Conclusion

We have shown how to compute the energy spectrum of two-particle scattering in non-relativistic quantum mechanics in a box with periodic boundary conditions. We do not discretize the box into a lattice. Instead, we employ a three-dimensional cartesian Fourier basis to diagonalize the Hamiltonian, which is treated block by block. It requires a group-theoretical projection of the Fourier basis into sectors that transform according to the irreducible representations of the symmetry group under consideration. These irreducible representations are the natural vehicles in which angular momentum is resolved in the box. We considered four scattering scenarios that are of current interest. For spin-0 system in cubic box, it involves the octahedral group O_h and its 10 irreducible representations $A_1^{\pm}$, $A_2^{\pm}$, $E^{\pm}$, $T_1^{\pm}$, $T_2^{\pm}$. For spin-1/2 system in cubic box, it involves the ${}^2O_h$ group and its six half-integer irreducible representations $G_1^{\pm}$, $G_2^{\pm}$, and $H^{\pm}$. For spin-0 system in elongated box, it involves the dihedral group D_{4h} and its 10 irreducible representations $A_1^{\pm}$, $A_2^{\pm}$, $B_1^{\pm}$, $B_2^{\pm}$, $E^{\pm}$. For spin-1/2 system in cubic box, it involves the ${}^2D_{4h}$ group and its four half-integer irreducible representations $G_1^{\pm}$ and $G_2^{\pm}$. The projected Fourier basis in each case is of general-purpose; they can be used for the block-diagonalization of any Hamiltonian system in a box. Convergent results for a hundred low-lying energy levels can be obtained quickly on a standard workstation or laptop using basis size on the order of a thousand. There is no difference in computation time for different boxes since the box size L (or η) is adjusted as a single parameter. This is an advantage over the lattice method which scales like N^3 in changing the volume. Using simple test potentials, we demonstrated how the various bound and scattering states in the infinite volume are resolved in the periodic box. Although elongated boxes are less visually appealing in the identification of resonances in stabilization diagrams, they are expected to be just as effective as cubic boxes in numerical analysis via the Lüscher method. Elongated boxes do offer an advantage in terms of cost-effectiveness in lattice simulations where the box is discretized into a three-dimensional periodic lattice. In such scenarios, the cost of elongation is proportional to N_z whereas the cost of changing the cubic volume grows with $N_x N_y N_z$.

Sufficient details are given both in the write-up and in the package on how the calculation is carried out. It is structured in a way that is relatively straightforward to modify for new physics projects. We envision the package to be useful in a number of ways. It can be a pedagogical tool for students who are learning how to apply group theory in numerical projects under a box geometry. It can be used to validate

phaseshift formulas (or quantization conditions) that are projected according to the same irreps of the box, particularly those for half-integer spin in elongated boxes.[7] Conventionally these formulas are treated in a self-consistent manner: they are used to predict phaseshifts given the energies, but also "reverse-engineered" to infer the energy spectrum from the targeted phaseshifts. A potential model can provide an independent check of the formulas. The package can also be used to inform the design of lattice QCD simulations. Systems can be model-tested in a box in simple quantum mechanics before a full-fledged lattice QCD simulation is embarked upon. Aspects such as kinematic coverage, irrep channel selection, and pion mass dependence can all be investigated on a laptop. Such a study to model the delta resonance in pion-nucleon scattering is under way. Finally, given the challenge of lattice QCD simulation of three-body systems, a model numerical study in the box applying similar techniques in this package could be beneficial.

Acknowledgements

F.X.L. and A.A. are supported in part by the U.S. Department of Energy grant DE-FG02-95ER40907. C.M. is supported in part by the National Science Foundation grant PHY-1913158.

Appendix A. Infinite-volume Solutions

In infinite volume, the Schödinger equation in Eq. (1) with the central potential $V(r)$ admits solutions with spherical symmetry. The solution in spherical coordinate can be expanded in partial waves $\psi(\boldsymbol{r}) = \sum_l R_l(r) Y_{lm}(\theta, \phi)$ where Y_{lm} is spherical harmonics. The radial wavefunction $R_l(r)$ satisfies the standard equation,

$$\left[-\frac{\hbar^2}{2\mu} \frac{d^2}{dr^2} + \frac{l(l+1)\hbar^2}{2\mu r^2} + V(r) \right] u_l(r) = E u_l(r), \tag{A.1}$$

where $u_l(r) = r R_l(r)$ is the auxiliary radial wavefunction. Depending on the potential, the solution can be bound states whose energies are quantized, or scattering states whose energy are continuous. The boundary conditions for bound states are $u(r)$ must vanish at the origin and large distances. For scattering states the boundary conditions are

$$\lim_{r\to 0} u_l(r) = 0 \quad \text{and} \quad \lim_{r\to\infty} u_l(r) \propto e^{i\delta_l} \sin\left[kr - \frac{l\pi}{2} + \delta_l \right], \tag{A.2}$$

where $k = \sqrt{2\mu E/\hbar^2}$ is the relative back-to-back CM momentum and δ_l is the phaseshift for partial-wave l. The presence of the $-l\pi/2$ term is to account for the centrifugal barrier term $\frac{l(l+1)\hbar^2}{2\mu r^2}$ and is inserted to ensure that the phaseshift in this definition vanishes when the potential itself vanishes. Conventionally, to obtain the phaseshift it is necessary to solve a second-order differential equation from the origin

to the asymptotic region, then match the solution with an appropriate sine function. Here we resort to the *variable phase method*[17] which requires solving only a first-order differential equation,

$$\frac{d\tilde{\delta}_l(k,r)}{dr} = -\frac{U(r)}{k}[\cos\tilde{\delta}_l(k,r)\hat{j}_l(kr) - \sin\tilde{\delta}_l(k,r)\hat{n}_l(kr)]^2, \tag{A.3}$$

where $U(r) = \frac{2\mu}{\hbar^2}V(r)$. The phase function $\tilde{\delta}_l(k,r)$ is integrated from the origin where $\tilde{\delta}_l(k,0) = 0$ to the asymptotic region where the potential is negligible; then the scattering phaseshift is obtained directly as the asymptotic value $\delta_l(k) = \lim_{r\to\infty}\tilde{\delta}_l(k,0)$. A few salient features of the method are worth pointing out. (1) The physical meaning of the phase equation is clear: It describes the accumulation of the phaseshift due to the potential from zero to its asymptotic value. If the potential does not change sign, the asymptotic value is reached monotonically. In the limit of zero potential strength, the phaseshift vanishes. (2) The physical meaning of the phase function also becomes apparent: The value of $\tilde{\delta}_l(k,0)$ at distance r from the origin is the scattering phaseshift that would be produced by the potential if it were truncated beyond r. (3) The phaseshift from this method does not suffer from the mod(π) ambiguity inherent in Eq. (A.2) and is a continuous function of the momentum k. (4) The overall negative sign signifies a well-known result in scattering: Repulsive (positive) potentials produce negative phaseshifts; attractive (negative) potentials produce positive phaseshifts. (5) The negative sign also implies a formal symmetry of the phase function if we change the sign of momentum k, namely $\delta_l(k,r) = -\delta_l(-k,r)$ (where we added the k-dependence) which leads to the well-known property of the S-matrix, $S_l(k,r) = S_l^{-1}(-k,r)$. (6) At high energies, the $1/k$ factor guarantees that the phaseshift vanishes, $\lim_{k\to\infty}\delta_\ell = 0$. In the limit of zero energy, the phaseshift satisfies Levinson's theorem $\lim_{k\to 0}\delta_\ell = n_b\pi$, where n_b is the number of bound states in the ℓth partial wave. The exception is when a zero-energy s-wave resonance occurs, in which case Levinson's theorem is modified to $\lim_{k\to 0}\delta_0 = (n_b + 1/2)\pi$ (we did not encounter such a case in this study). Levinson's theorem is an index theorem that can reveal the number of bound states purely from the behavior of the phaseshifts at low and high energy limits.

To get a landscape view, the test potentials for the two systems in this study, Eqs. (2) and (3), are plotted together in Fig. A.1 for a number of partial waves. The black curves correspond to the spin-0 potential $V(r)$ in Eq. (2); the blue curves to the spin-1/2 potential $V_{J=l+\frac{1}{2}}(r)$ in Eq. (6); and the red curves $V_{J=l-\frac{1}{2}}(r)$ in Eq. (7). T he spin-orbit coupling coefficient is chosen as $c_{\ell s} = 1.0$. Note that for s-wave, $V(r)$ and $V_{J=l+\frac{1}{2}}(r)$ are degenerate, while $V_{J=l-\frac{1}{2}}(r)$ not defined. The range of the potentials extends to a distance of about $r = 8$. The centrifugal barrier pushes the effective range further out with increasing partial wave.

In Fig. A.2, we display the phaseshifts and their derivatives computed from the variable phase method for the spin-0 potential. The gridlines indicating multiples of π are draw for the phaseshifts. From the values at $E \to 0$, we can predict the number of bound states via the Levinson's theorem: there are two bound states in the s-wave,

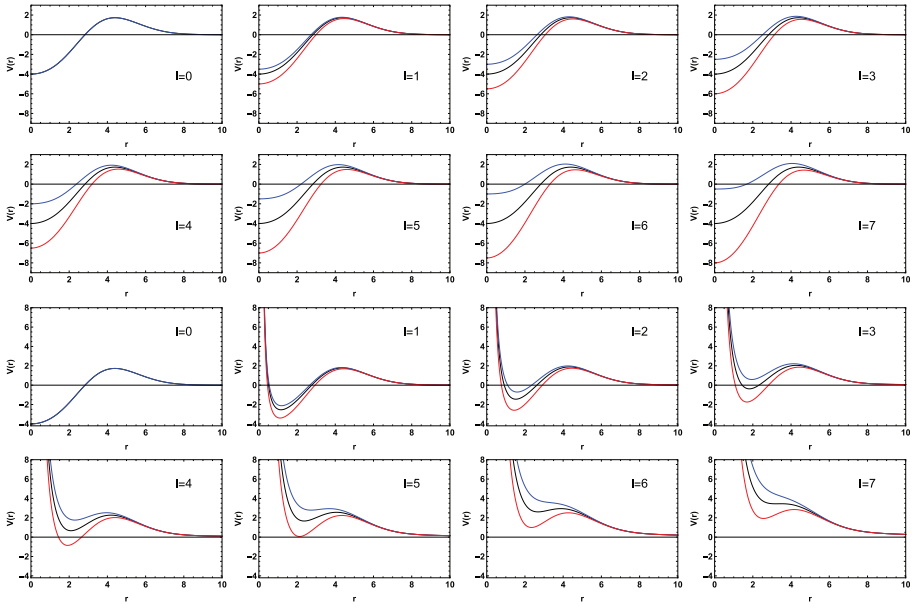

Fig. A.1. (Color online) Plot of the test potentials as a function of distance for partial waves up to $l = 7$. The three curves correspond to spin-0 potential (black), spin-/12 potential $V_{J=l+\frac{1}{2}}(r)$ (blue), and spin-1/2 potential $V_{J=l-\frac{1}{2}}(r)$ (red). Top two rows: just $V(r)$. Bottom two rows: $V(r)$ + centrifugal barrier term.

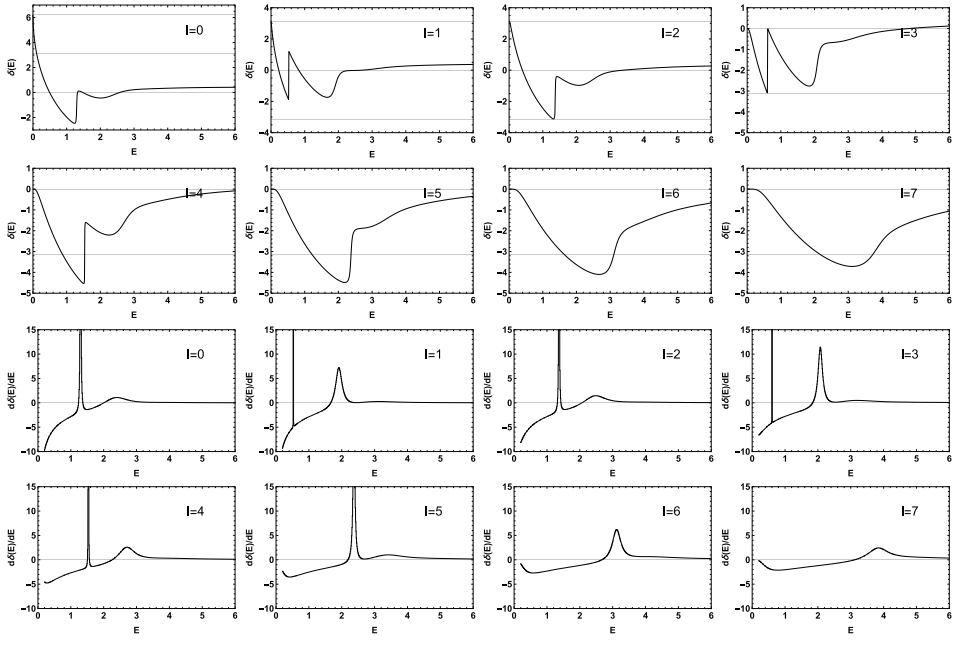

Fig. A.2. Top two rows: phaseshifts as a function of energy for the spin-0 potentials (black curves in Fig. A.1). Bottom two rows: derivative of phaseshifts. The gridlines indicate multiples of π.

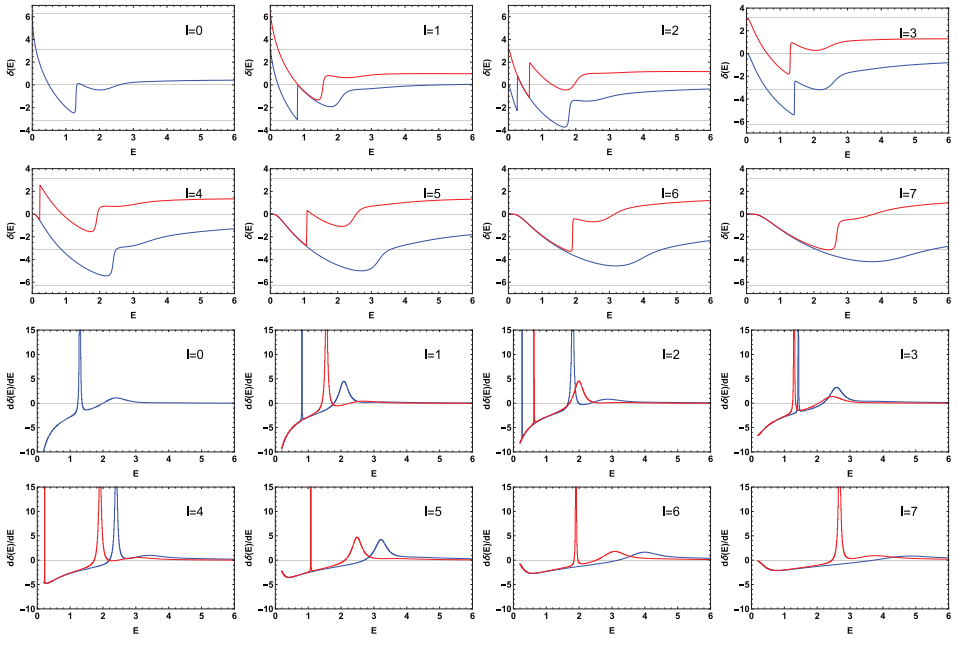

Fig. A.3. (Color online) Top two rows: phaseshifts as a function of energy for the spin-1/2 potentials (color-coded to correspond to blue and red curves in Fig. A.1). Bottom two rows: derivative of phaseshifts.

one in p-wave, one in d-wave, and no bound states in higher partial waves. This is corroborated by the effective potential (the black curve in Fig. A.1). In the $l = 3$ partial wave, it has a small negative dip but not enough to support a bound state. We use a Mathematica eigensolver to locate the bound states under Dirichlet boundary conditions. For scattering states, we are interested in resonances as signaled by sudden increases in the phaseshifts, or as peaks in the first derivative of the phaseshift. We see some very sharp resonances in the lower partial waves. Each partial wave has a sharp resonance followed by a broad one. The derivative curves can be modeled by a resonant Breit–Wigner term and a slowly-varying background,

$$\frac{d\delta_l(E)}{dE} = \frac{\Gamma/2}{(E_r - E_r)^2 + \Gamma^2/4} + c_0 + c_1 E + c_2 E^2 + c_3 E^3, \tag{A.4}$$

where E_r is the pole position Γ the width. This form does not work well with extremely sharp resonances. In such cases, the pole position and width can be estimated by inspecting the peaks on a detailed plot.

Figure A.2 depicts the situation in the spin-1/2 system. In the $J = l + \frac{1}{2}$ channel (blue) which is made shallower by the spin-orbit term, there are two bound states in the s-wave, one in p-wave, according to Levinson's theorem. In the $J = l - \frac{1}{2}$ channel (red) which is made deeper by the spin-orbit term, there are two bound states in the

s-wave, two in p-wave, one in d-wave. In fact, there is a very shallow bound state $E = -0.061$ that is missed by Levinson's theorem (due to numerical inaccuracies in computing the phaseshift), but caught by the eigensolver. As for scattering states, the basic feature of a sharp resonance followed by a broader one persists in both channels. The deeper channel induces two sharp resonances below $E = 3$ in higher partial waves ($l = 6, 7$). More interestingly, there are two extremely sharp resonances just above threshold ($E = 0.262$ in $l = 2$ and $E = 0.225$ in $l = 3$).

The combined spectra of bound and scattering states are displayed in the main text in Fig. 1 for the spin-0 system, and Fig. 2 for the spin-1/2 system.

Appendix B. Cross Check of Energy Spectrum by Lüscher's Method

Lüscher established exact relations (called quantization conditions or QC) between elastic scattering phaseshifts in the infinite-volume and the two-body energy spectrum enclosed in a periodic box.[2] In general, the QC has couplings to an infinite tower of partial waves and does not have predictive power for phaseshifts. However, if all higher partial waves but the lowest one can be neglected, it can be used to predict the phaseshift of the lowest partial wave given the energy in the box. This is often referred to as the Lüscher method. Here, we perform such a study using the energy spectrum for the A_1^+ irrep in the cubic box as an example. The A_1^+ irrep couples to partial waves $\ell = 0, 4, 6, \ldots$ so it can be used to predict the s-wave phaseshift via the equation,

$$\cot \delta_0(k) = \frac{\mathcal{Z}_{00}(q^2, L)}{\pi^{3/2} q} \quad \text{with } q \equiv \frac{kL}{2\pi}. \tag{B.1}$$

Here $\mathcal{Z}_{00}$ is a zeta function whose general definition is given by a sum over integers,

$$\mathcal{Z}_{lm}(q^2, L) = \sum_{\boldsymbol{n}=\{n_1,n_2,n_3\}} \frac{n^l Y_{lm}(\theta, \phi)}{n^2 - q^2}. \tag{B.2}$$

It has poles at $q^2 = n^2$ which are the noninteracting (free-particle) energies in the box. By feeding the discrete interacting k obtained in a box of size L into Eq. (B.1), $\delta_0(k)$ can be obtained and compared to that in the infinite volume displayed in Fig. A.2. The prediction is expected to be valid for low energies where the lower partial waves dominate and box size $L > 2R$ where R is the range of the interaction. Figure B.1 shows the result of such an comparison for four box sizes. The range displayed in momentum k of 0 to 0.8 corresponds to energy E of 0 to 1.265. The pole in the infinite-volume result (black curve) is due to the sharp resonance present in this channel. We see good agreement in the low energy region. The larger boxes provide more points and reach lower in energy. The agreement deteriorates at higher energies, which we attribute to the higher partial waves that are cut off in the Lüscher method. Though a limited comparison study, it demonstrates the efficacy of the Lüscher method and the extent to which it applies, at least for the toy potential model employed in this work.

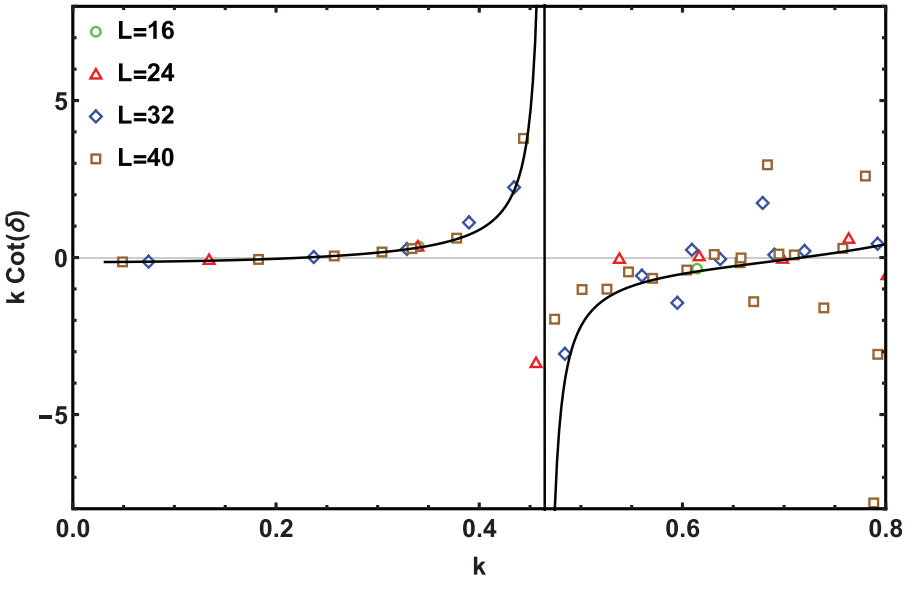

Fig. B.1. (Color online) Phaseshift predicted from the Lüscher method in the cubic box (colored points) is compared to that from the infinite-volume (black curve) in the A_1^+ irrep of the cubic box.

Appendix C. Matrix Elements

The Fourier integrals in Eq. (14) can be carried out analytically for the test potentials. The overlap term is separable into a product,

$$\langle \gamma' n_x' n_y' n_z' | \gamma n_x n_y n_z \rangle = \int_{-L/2}^{L/2} dx\, \phi_{n_x'}(\gamma', x)\phi_{n_x}(\gamma, x) \int_{-L/2}^{L/2} dy\, \phi_{n_y'}(\gamma', y)\phi_{n_y}(\gamma, y) \times \int_{-L/2}^{L/2} dz\, \phi_{n_z'}(\gamma', z)\phi_{n_z}(\gamma, z). \tag{C.1}$$

The basis function in x-direction with the damping factor $e^{-\gamma x^2}$ can be concisely written as

$$\phi_{n_x}(\gamma, x) = Z(n, L) f_n(K(n, L)x) e^{-\gamma x^2}, \tag{C.2}$$

where the functions are defined as

$$K(n, L) \equiv \frac{\pi}{L}\left[n + \frac{1}{2}(1 - (-1)^n)\right] (n = 0, 1, 2, \ldots), \quad Z(n, L) \equiv \sqrt{\frac{2}{L(1 + \delta_{n0})}},$$
$$f_n(x) \equiv \begin{cases} \cos(x) & n \text{ even}, \\ \sin(x) & n \text{ odd}. \end{cases} \tag{C.3}$$

The $K(n, L)$ function will be used, but the $Z(n, L)$ and $f_n(x)$ functions are absorbed into new functions below. The final result for the overlap is given in closed form by

$$\langle \gamma' n_x' n_y' n_z' | \gamma n_x n_y n_z \rangle = \Omega^{(0)}_{n_x' n_x}(\tau) \Omega^{(0)}_{n_y' n_y}(\tau) \Omega^{(0)}_{n_z' n_z}(\tau). \tag{C.4}$$

The kinetic energy term is also separable and the final result is given by

$$\begin{aligned}\langle\gamma' n'_x n'_y n'_z|T|\gamma n_x n_y n_z\rangle &= \frac{1}{2}[6\gamma + K^2(n_x,L) + K^2(n_y,L) + K^2(n_z,L)]\Omega^{(0)}_{n'_x n_x}(\tau)\\ &\times\ \Omega^{(0)}_{n'_y n_y}(\tau)\Omega^{(0)}_{n'_z n_z}(\tau) + \gamma L[K(n_x,L)\Omega^{(1)}_{n'_x n_x}(\tau)\Omega^{(0)}_{n'_y n_y}(\tau)\Omega^{(0)}_{n'_z n_z}(\tau)\\ &+\ K(n_y,L)\Omega^{(0)}_{n'_x n_x}(\tau)\Omega^{(1)}_{n'_y n_y}(\tau)\Omega^{(0)}_{n'_z n_z}(\tau) + K(n_z,L)\Omega^{(0)}_{n'_x n_x}(\tau)\Omega^{(0)}_{n'_y n_y}(\tau)\Omega^{(1)}_{n'_z n_z}(\tau)]\\ &-\ \frac{1}{2}\gamma^2 L^2[\Omega^{(2)}_{n'_x n_x}(\tau)\Omega^{(0)}_{n'_y n_y}(\tau)\Omega^{(0)}_{n'_z n_z}(\tau) + \Omega^{(0)}_{n'_x n_x}(\tau)\Omega^{(2)}_{n'_y n_y}(\tau)\Omega^{(0)}_{n'_z n_z}(\tau)\\ &+\ \Omega^{(0)}_{n'_x n_x}(\tau)\Omega^{(0)}_{n'_y n_y}(\tau)\Omega^{(2)}_{n'_z n_z}(\tau)]. \end{aligned} \tag{C.5}$$

The final result for the potential energy $V(r) = (-V_0 + V_1 r^4)e^{-\beta r^2}$ is given by

$$\begin{aligned}\langle\gamma' n'_x n'_y n'_z|V|\gamma n_x n_y n_z\rangle &= -V_0\Omega^{(0)}_{n'_x n_x}(a)\Omega^{(0)}_{n'_y n_y}(a)\Omega^{(0)}_{n'_z n_z}(a)\\ &-\ \frac{1}{16}V_1 L^4[\Omega^{(4)}_{n'_x n_x}(a)\Omega^{(0)}_{n'_y n_y}(a)\Omega^{(0)}_{n'_z n_z}(a) + \Omega^{(0)}_{n'_x n_x}(a)\Omega^{(4)}_{n'_y n_y}(a)\Omega^{(0)}_{n'_z n_z}(a)\\ &+\ \Omega^{(0)}_{n'_x n_x}(a)\Omega^{(0)}_{n'_y n_y}(a)\Omega^{(4)}_{n'_z n_z}(a) + 2\Omega^{(2)}_{n'_x n_x}(a)\Omega^{(2)}_{n'_y n_y}(a)\Omega^{(0)}_{n'_z n_z}(a)\\ &+\ 2\Omega^{(2)}_{n'_x n_x}(a)\Omega^{(0)}_{n'_y n_y}(a)\Omega^{(2)}_{n'_z n_z}(a) + 2\Omega^{(0)}_{n'_x n_x}(a)\Omega^{(2)}_{n'_y n_y}(a)\Omega^{(2)}_{n'_z n_z}(a)]. \end{aligned} \tag{C.6}$$

They are expressed in terms of a super-function defined by,

$$\Omega^{(A)}_{n'n}(\alpha) \equiv Z(n',n)[I_A(\alpha, b_-(n',n)) + (-1)^{n+A} I_A(\alpha, b_+(n',n))], \tag{C.7}$$

where

$$Z(n',n) \equiv \frac{1}{4}[1 + (-1)^{n'+n}]\sqrt{\frac{1}{(1+\delta_{n'0})}}\sqrt{\frac{1}{(1+\delta_{n0})}}, \tag{C.8}$$

and

$$b_\pm(n',n) \equiv \frac{L}{2}[K(n',L) \pm K(n,L)], \tag{C.9}$$

are pure functions of integers (L cancels in $b_\pm(n',n)$ function). The variables τ and a represent the following combinations (linear in L),

$$\tau = \frac{L}{2}\sqrt{\beta+\gamma+\gamma'}, \quad a = \frac{L}{2}\sqrt{\gamma+\gamma'}. \tag{C.10}$$

The four integrals are defined by

$$\begin{aligned} I_0(a,b) &= \int_{-1}^{1} dx\ \cos(bx)e^{-a^2x^2},\\ I_1(a,b) &= \int_{-1}^{1} dx\, x\ \sin(bx)e^{-a^2x^2},\\ I_2(a,b) &= \int_{-1}^{1} dx\, x^2\ \cos(bx)e^{-a^2x^2},\\ I_4(a,b) &= \int_{-1}^{1} dx\, x^4\ \cos(bx)e^{-a^2x^2}, \end{aligned} \tag{C.11}$$

whose evaluations involve the error function $\mathrm{erf}(x) = \int_{-x}^{x} dt\, e^{-t^2}$.

Note that the introduction of the damping factor $e^{-\gamma x^2}$ to the basis functions can cause the overlap to become positive nondefinite, especially for small box sizes (when L is close to the range of the potential). In such cases, a single value decomposition (SVD) is used to project out the bad subspace in the overlap matrix. Construction of the Hamiltonian matrix is the most costly part of the calculation. For improved speed, the evaluation of the matrix elements is done by C++ code whose execution is seamlessly called from inside Mathematica.

In the case of elongated box $L \times L \times L\eta$ with η the elongation factor in the z-direction, the z integration receives special treatment in Eqs. (40) and (41). The corresponding results become functions of both L and η instead of just L. The transition is fairly straightforward. The $Z(n', n)$ and $b_{\pm}(n', n)$ functions remain the same. The $K(n, L)$, τ and a functions receive the substitution $L \to L\eta$ in the z-direction. At the same time, the super-function $\Omega^{(A)}$ is rescaled by the factor η^A from the explicit L factors appearing in Eqs. (C.5) and (C.6). Applying these substitutions, the overlap term is given by

$$\langle \gamma' n'_x n'_y n'_z | \gamma n_x n_y n_z \rangle = \Omega^{(0)}_{n'_x n_x}(\tau) \Omega^{(0)}_{n'_y n_y}(\tau) \Omega^{(0)}_{n'_z n_z}(\tau\eta). \tag{C.12}$$

The kinetic energy term is given by

$$\begin{aligned}
\langle \gamma' n'_x n'_y n'_z | T | \gamma n_x n_y n_z \rangle = {} & \frac{1}{2}[6\gamma + K^2(n_x, L) + K^2(n_y, L) + K^2(n_z, L\eta)] \Omega^{(0)}_{n'_x n_x}(\tau) \\
& \times \Omega^{(0)}_{n'_y n_y}(\tau) \Omega^{(0)}_{n'_z n_z}(\tau\eta) + \gamma L [K(n_x, L) \Omega^{(1)}_{n'_x n_x}(\tau) \Omega^{(0)}_{n'_y n_y}(\tau) \Omega^{(0)}_{n'_z n_z}(\tau\eta) \\
& + K(n_y, L) \Omega^{(0)}_{n'_x n_x}(\tau) \Omega^{(1)}_{n'_y n_y}(\tau) \Omega^{(0)}_{n'_z n_z}(\tau\eta) + \eta\, K(n_z, L\eta) \Omega^{(0)}_{n'_x n_x}(\tau) \Omega^{(0)}_{n'_y n_y}(\tau) \\
& \times \Omega^{(1)}_{n'_z n_z}(\tau\eta)] - \frac{1}{2}\gamma^2 L^2 [\Omega^{(2)}_{n'_x n_x}(\tau) \Omega^{(0)}_{n'_y n_y}(\tau) \Omega^{(0)}_{n'_z n_z}(\tau\eta) + \Omega^{(0)}_{n'_x n_x}(\tau) \Omega^{(2)}_{n'_y n_y}(\tau) \\
& \times \Omega^{(0)}_{n'_z n_z}(\tau\eta) + \eta^2 \Omega^{(0)}_{n'_x n_x}(\tau) \Omega^{(0)}_{n'_y n_y}(\tau) \Omega^{(2)}_{n'_z n_z}(\tau\eta)].
\end{aligned} \tag{C.13}$$

The result for the potential energy $V(r) = (-V_0 + V_1 r^4) e^{-\beta r^2}$ is given by

$$\begin{aligned}
\langle \gamma' n'_x n'_y n'_z | V | \gamma n_x n_y n_z \rangle = {} & -V_0 \Omega^{(0)}_{n'_x n_x}(a) \Omega^{(0)}_{n'_y n_y}(a) \Omega^{(0)}_{n'_z n_z}(a\eta) \\
& + \frac{1}{16} V_1 L^4 [\Omega^{(4)}_{n'_x n_x}(a) \Omega^{(0)}_{n'_y n_y}(a) \Omega^{(0)}_{n'_z n_z}(a\eta) + \Omega^{(0)}_{n'_x n_x}(a) \Omega^{(4)}_{n'_y n_y}(a) \Omega^{(0)}_{n'_z n_z}(a\eta) \\
& + \eta^4\, \Omega^{(0)}_{n'_x n_x}(a) \Omega^{(0)}_{n'_y n_y}(a) \Omega^{(4)}_{n'_z n_z}(a\eta) + 2\, \Omega^{(2)}_{n'_x n_x}(a) \Omega^{(2)}_{n'_y n_y}(a) \Omega^{(0)}_{n'_z n_z}(a\eta) \\
& + 2\eta^2\, \Omega^{(2)}_{n'_x n_x}(a) \Omega^{(0)}_{n'_y n_y}(a) \Omega^{(2)}_{n'_z n_z}(a\eta) + 2\, \eta^2\, \Omega^{(0)}_{n'_x n_x}(a) \Omega^{(2)}_{n'_y n_y}(a) \Omega^{(2)}_{n'_z n_z}(a\eta)].
\end{aligned} \tag{C.14}$$

The spin-1/2 system is handled in a similar fashion. If a different potential is desired, only the potential part needs to be re-coded. The overlap and kinetic terms remain the same.

References

1. A. U. Hazi and H. S. Taylor, *Phys. Rev. A* **1**, 1109 (1970).
2. M. Lüscher, *Nucl. Phys. B* **354**, 531 (1991).

3. K. Rummukainen and S. A. Gottlieb, *Nucl. Phys. B* **450**, 397 (1995), arXiv:hep-lat/9503028 [heplat].
4. M. Gockeler, R. Horsley, M. Lage, U. G. Meissner, P. E. L. Rakow, A. Rusetsky, G. Schierholz and J. M. Zanotti, *Phys. Rev. D* **86**, 094513 (2012), arXiv:1206.4141 [hep-lat].
5. T. Luu and M. J. Savage, *Phys. Rev. D* **83** (2011), doi: 10.1101/phyrevd.83.114508.
6. X. Feng, X. Li and C. Liu, *Phys. Rev. D* **70**, 014505 (2004), arXiv:hep-lat/0404001 [heplat].
7. F. X. Lee and A. Alexandru, *Phys. Rev. D* **96**, 054508 (2017), arXiv:1706.00262 [hep-lat].
8. R. A. Briceno, *Phys. Rev. D* **89**, 074507 (2014), arXiv:1401.3312 [hep-lat].
9. C. Morningstar, J. Bulava, B. Singha, R. Brett, J. Fallica, A. Hanlon and B. Hörz, *Nucl. Phys. B* **924**, 477 (2017), arXiv:1707.07817 [hep-lat].
10. Y. Li, J.-J. Wu, C. D. Abell, D. B. Leinweber and A. W. Thomas, Partial wave mixing in hamiltonian effective field theory, arXiv:1910.01971 [hep-lat].
11. M. T. Hansen and S. R. Sharpe, *Phys. Rev. D* **95**, 034501 (2017).
12. M. Mai, M. Döring, C. Culver and A. Alexandru, Three-body unitarity versus finite-volume $\pi^+\pi^+\pi^+$ spectrum from lattice qcd, arXiv:1909.05719 [hep-lat]
13. R. A. Brice no, M. T. Hansen and A. W. Jackura, Consistency checks for two-body finite-volume matrix elements: I. Conserved currents and bound states, arXiv:1909.10857 [hep-let].
14. D. Guo, A. Alexandru, R. Molina and M. Döring, *Phys. Rev. D* **94**, 034501 (2016), arXiv:1605.03093 [hep-lat].
15. C. Culver, M. Mai, A. Alexandru, M. Döring and F. X. Lee, *Phys. Rev. D* **100**, 034509 (2019), arXiv:1905.10202 [hep-lat].
16. J. Bulava, Meson-nucleon scattering amplitudes from lattice qcd, arXiv:1909.13097 [hep-lat].
17. F. Calogero, *Variable Phase Approach to Potential Scattering* (Academic Press, New York, 1967).